Title

Simplified Multi-scale Modeling of Laser Powder Bed Fusion Additive Manufacturing Processes

Permalink

https://escholarship.org/uc/item/4416w5td

Author

Mehraban Teymouri, Raeita

Publication Date

2022

Peer reviewed|Thesis/dissertation

Simplified Multi-scale Modeling of Laser Powder Bed Fusion Additive Manufacturing Processes

By

RAEITA MEHRABAN TEYMOURI
DISSERTATION

Submitted in partial satisfaction of the requirements for the degree of

DOCTOR OF PHILOSOPHY

in

Mechanical and Aerospace Engineering

in the

OFFICE OF GRADUATE STUDIES

of the

UNIVERSITY OF CALIFORNIA

DAVIS

Approved:

_____
Bahram Ravani, Chair

_____
Barbara Linke

_____
Jean-Pierre Delplanque

Committee in Charge

2022

Abstract

Additive Manufacturing (AM) or 3D printing of metals has been expanding into a variety of different industrial sectors due to its many advantages which include but are not limited to fabrication of geometrically complex metallic components and minimal material waste. Laser Powder Bed Fusion (LPBF) processes are one of the most prominent metal AM technologies of the recent years. However, despite its unlimited potential, LPBF process has a chaotic nature with complex interactions and dependencies. Therefore, researchers have faced many challenges in accurately and efficiently capturing the complex micro-length and time scale phenomena in modeling this process through numerical approaches.

Lack of control of the temperature field in the LPBF process would lead to microstructural, surface quality and structural defects during printing. After a comprehensive literature review, this research has identified two major categories of thermal modeling approaches for LPBF processes. The first group is based on thermo-fluid simulations, also called Computational Fluid Dynamics (CFD) simulations that couple fluid dynamics and heat transfer. Due to their high computational costs, these high-fidelity models are usually limited to a single or very few scanning tracks. The second group of thermal modeling techniques are based on efficient yet over-simplified conduction-only models that neglect melt-pool dynamics. Although the efficiency of these models makes them suitable for multi-layer modeling, their predictions are not accurate and hence would lead to subsequent poorly defined thermo-mechanical and microstructure modeling. Therefore, this dissertation develops a novel numerical approach that would efficiently account for major micro-scale phenomena in multi-layer simulations of the LPBF processes.

In this dissertation, a Simplified Multi-scale Modeling (SMM) approach is presented to bridge the aforementioned numerical techniques accounting for lower length scale phenomena while allowing to conveniently scale up to larger domains for LPBF simulations. The thermal component of the SMM approach is the Comprehensive Thermal Model (CTM) which has multiple unique features that include numerical implementation of fluid flow effects (namely, evaporation, Marangoni convection, and process-induced micro-voids), process and material dependent absorptivity, latent heat, and phase transition effects, and temperature-dependent thermo-physical properties for bulk and powder material.

The CTM is shown to be more accurate than a simplified conduction-only thermal model and more efficient than computationally expensive CFD simulations. The CTM developed is successfully verified through comparison with experimental temperature measurements from literature and then used as a computational tool to predict the thermal signature histories, surface cooling rates, and melt-pool dimensions for five of the most prominent AM alloys which are IN718, IN625, stainless steel 316L, Ti-6Al-4V, and AlSi10Mg. However, the proposed framework can also easily be extended to a wide range of alloys provided sufficient information is available.

With its efficiency and accuracy for multi-layer modeling, the SMM can be used as a computational experiment for studying process variability and printability of different material systems. The presented model could also be used to extract datasets for developing data-driven and physics-informed Reduced-Order Models (ROMs) that have better computational performance compared to conventional numerical approaches and could serve as a building block of a digital twin of the AM process.

Acknowledgements

First and foremost, I wanted to express my most sincere gratitude to my advisor Prof. Bahram Ravani for suggesting the topic of this dissertation and for his continuous guidance, support and encouragement throughout my doctorate studies. I would also like to give my warmest thanks to Dr. Chinnapat Panwisawas for his consistent guidance and feedback throughout this work. Without their excellent supervision this work could not be accomplished. I would also like to thank Dr. Barbara Linke and Dr. Jean-Pierre Delplanque who agreed to serve on my dissertation committee.

This research work was conducted as part of the UC-Davis contributions to the International Research Training Group (IRTG) 2057 under the directorship of Prof. Ravani in partnership with the University of Kaiserslautern in Germany funded by The German Research Foundation DFG (Deutsche Forschungs Gemeinschaft). I would like to thank all IRTG2057 members for their insightful comments and guidance through my Ph.D. study.

I would like to acknowledge the opportunities and funding provided by UC Davis through my graduate studies in the Mechanical and Aerospace Engineering department. I am grateful to my fellow lab members, collaborators, and other staff at the Advanced Highway Maintenance and Construction Technology (AHMCT) center for their help through my research work. Also, many thanks to all my friends and colleagues for their sincere support and encouragement through my graduate studies.

I would like to express my deepest gratitude to my dearest parents and brothers, Ramtin and Raein. Words cannot express how grateful I am for all of the sacrifices that they have made on my behalf. Last but not least, I want to thank my fiancé, Dr. Khosrow Dinyaryan, for his continuous support and endless love that kept me motivated throughout this research work.

Table of Contents

List of Figures

List of Tables

Chapter 1.   Introduction

Additive Manufacturing (AM) or 3D printing is a manufacturing process that involves layer-by-layer fabrication of 3D objects. AM allows for printing parts that are otherwise difficult or even impossible to construct using conventional subtractive machining approaches. Introduction of metal AM in the late 1980s was made a revolution in the era of manufacturing of parts with applications in many industries. With its profound advantages and capabilities, metal AM offers an ideal method for printing complex and customized metallic parts with substantial precision and control. According to [1], as of 2020, 54% of the metal AM market was possessed by Laser Powder Bed Fusion (LPBF) processes which makes the technology the most used metal AM technology worldwide.

Despite its wide popularity, LPBF is a highly complex and chaotic process which makes the fabrication of defect-free and high-quality parts an inherently difficult task. Simulating LPBF processes, and other metal AM technologies in general, has gained increasing attention from academia and industry as a practical way to improve the quality of the printed parts while avoiding conducting costly experiments. However, because of its process complexity, accurately simulating LPBF processes requires computationally expensive high-fidelity multi-scale multi-physics modeling to capture micro-length and time scale phenomena during the evolution of the material.

This chapter aims to introduce the challenges and importance of modeling LPBF processes as well as how this dissertation contributes to solving such problems (see Sections 1.1 and 1.2). Also, to enhance the readability a detailed description of the organization of this dissertation is included in Section 1.3.

1.1.   Motivation and Problem Statement

An accurate and efficient model of the transient temperature field is the foundation for modeling the microstructural evolution of the part and understanding its final properties. Moreover, high thermal gradients and cooling rates result in undesired thermal distortions and residual stresses that could even lead to crack formation in the fabricated parts. Therefore, accurate prediction of the temperature field during LPBF processes is critical as it enables preventing several detrimental defects in the printed parts. Predicting the thermomechanical response of the material during printing requires coupling the thermal model with a mechanical model.

Traditionally, two main approaches have been used to model the transient temperature field during LPBF processes: high-fidelity thermo-fluid models (or Computational Fluid Dynamics simulations) and macroscopic conduction-only thermal models. CFD simulations of the LPBF process can accurately capture the evolution of the material, from powder to final part, as they account for melt-pool fluid dynamics during scanning. These models are undoubtedly very accurate and commonly used in characterizing micro-length scale defects. However, because of their high computational costs as well as high computer power and memory requirements, these models are limited to a single or very few tracks. Therefore, such models are impractical in modeling the multi-layer process at the larger scale. On the other hand, existing macroscopic thermal simulations of the LPBF process are oversimplified and fail to consider major fluid flow effects, such as evaporation, Marangoni convection, and process-induced micro-voids.

To address such issues, this dissertation presents a modeling framework that effectively and efficiently links high-fidelity CFD simulations and macroscopic models for multi-track

multi-layer LPBF processes. The proposed approach is also used as a computational tool to study the dependence of the thermal history signatures, surface cooling rates, and melt-pool dimensions for some of the common commercially available AM alloys. The predictive capabilities of the model are verified through comparison with experimental measurements and the potential of the framework to be used for close loop control systems and AM digitalization is discussed.

1.2.   Contributions of this Work

The simplified multi-scale modeling framework developed in this dissertation is based on the comprehensive thermal model which is unique in multiple aspects. Firstly, it numerically accounts for major fluid flow effects (i.e., evaporation, Marangoni convection, process-induced micro-voids) while considering other effects such as process and material dependent absorptivity, latent heat, and phase transition effects as well as thermo-physical properties for bulk and powder material and heat loss due to radiation and natural convection. In other words, the model accounts for major lower length scale phenomena while enabling scaling up to larger domains of multi-track multi-layer LPBF simulations. Therefore, the presented thermal model serves as a more accurate and efficient alternative for the conventional modeling approaches of LPBF processes, i.e. high-fidelity CFD simulations and macroscopic conduction-only thermal models. It must be emphasized that implementation of the process-induced micro-voids is a novelty in this dissertation that provides a valuable first approximation to high-fidelity simulations and has potential to be further investigated in the future studies.

The accuracy of the proposed model makes it suitable to be used as the basis for mechanical and metallurgical coupled problems while the efficiency of the proposed model makes it practical in part-scale and structural level simulations. Therefore, the presented thermal

model can be effectively used to perform thermo-mechanical and microstructural sequentially coupled modeling. Computational efficiency and accuracy of the presented thermal model also make it a useful rapid computational tool that can be used to extract datasets from and develop process maps or even a reduced-order predictive model using deep learning techniques. A convolutional neural network architecture and physics-informed machine learning techniques that can be utilized for such purposes are proposed in this dissertation and can be further investigated to develop real-time simulation systems and digital twins of the AM process.

Lastly, a unique contribution of this dissertation is conducting a thorough material composition study to investigate the effects of material properties on the thermal history signatures, surface cooling rates, and melt-pool dimensions. In particular, multi-layer deposition of five of the most common AM alloys (i.e., IN718, IN625, stainless steel 316L, Ti-6Al-4V, and AlSi10Mg) are modeled and compared under the same amount of input energy.

1.3.   Organization of This Dissertation

This dissertation is organized into seven chapters. Chapter 1 (current chapter) introduces the problem statement and provides background information about the research problems that this dissertation aims to address. Chapter 2 starts with a comprehensive literature review of metal AM technologies, continues with the benefits and drawbacks of LPBF processes, and discusses existing modeling approaches for predicting the transient temperature field as well as the stress state and microstructure evolution. This chapter concludes with a survey of some of the most common commercially available simulation packages developed specifically for modeling metal AM processes and discusses their capabilities and limitations.

In Chapter 3, the simplified multi-scale modeling framework, developed in this dissertation, is presented and the different aspects of the thermal component of the approach are

discussed in detail. This chapter also discusses the simplifying assumptions utilized to increase the efficiency of the modeling approach while maintaining its accuracy and predictive capabilities. This chapter concludes with a description of how the sequentially coupled thermo-mechanical model is formulated in this dissertation as well as how reduced-order models can be integrated within this framework to increase computational efficiency. Chapter 4 presents and discusses the results obtained from multi-layer simulations of the alloys of interest. These results include thermal history signatures and peak temperatures, surface cooling rates, and melt-pool evolution during the five-layer deposition process. Chapter 5 compares the thermal history predictions of the numerical model with temperature measurements from experiments and successfully validates the presented thermal model. Chapter 6 discusses the significance of accounting for fluid flow effects, as one of the most critical features of the thermal model, for temperature and stress field predictions. Finally, Chapter 7 concludes with a summary of the current study and potential areas of future research in this field of work.

Chapter 2. Literature Review and Gap Analysis

2.1 <u>Metal Additive Manufacturing Technologies</u>

Currently, there are numerous metal AM processes. However, these AM processes fall into seven major categories, defined by the American Society for Testing and Materials (ASTM): Vat Photopolymerization (VP), Material Extrusion (ME), Directed Energy Deposition (DED), Material Jetting (MJ), Binder Jetting (BJ), Sheet Lamination (SL), and LPBF [1]. Figure 2.1 provides a graphical representation of these seven major metal AM technologies and their mechanisms.

Two AM processes of Digital Light Processing (DLP) and Stereolithography (SLA) fall under the VP category (both approaches are shown in Figure 2.1*Figure 2.1*(a)). Both processes involve exposing liquid material to light to cure it and turn it into solid material. The difference between the two technologies lies in the light source used. In SLA, Ultraviolet (UV) laser is used to cure the liquid material whereas in DLP a digital light projector is utilized. These processes offer high levels of accuracy and good surface finish. However, they are slow in nature and can be used to process a very limited range of materials. Also, it must be mentioned that VP processes can be used for printing partially metallic parts only. In other words, to print parts with partial metal content, it is essential to use composite resins that include metallic particles. As the first commercialized AM process, VP has come a long way to offer high resolution and accuracy compared to many of the existing AM processes [2]. In fact, most recently, this technology has been utilized to fabricate a wide range of functional materials such as battery active materials (e.g. lithium sulfide/carbon composites) [3].

ME is a manufacturing process that involves extrusion of melted material, in the form of a continuous filament, through a heated extruding nozzle (see Figure 2.1(b)). Fused Deposition

Modeling (FDM) and Bound Powder Extrusion (BPE) are two of the metal AM processes in the ME category. Due to low raw material waste, this unique AM technology allows for a cost-efficient production. However, one of the major drawbacks of this technology is its inability to print parts with strong mechanical properties. Recent studies have introduced new advancements in ME that allow for printing denser parts with better mechanical performance. Additionally, careful control and optimization of the process parameters, such as nozzle temperature and infill pattern, can significantly improve the quality and mechanical performance of the printed parts [4].

There are multiple processes that lie under the DED category. However, there are two distinct groups of DED processes in terms of energy: cold spray and thermal energy. In the cold spray process, the material is in the form of fine particles that are added to the substrate with sufficient kinetic energy such that a dense layer is created. Conversely, the printing technology behind thermal energy process mainly consists of a nozzle that deposits melted material onto the substrate (see Figure 2.1(c)). The material can be fed through the nozzle in the form of either powder or wire.

In MJ (as shown in Figure 2.1(d)), the printheads used have numerous inkjet nozzles that simultaneously jet or spray photopolymer resin onto the build plate. Then, UV light is applied to selectively cure the layer. This allows for printing parts that are geometrically complex and difficult to print with other AM processes. MJ also can result in robust properties for the final product and provides easy removal of support structures. However, this AM technology is limited in materials that can be used as well as the size of the printed parts. In order to produce metallic parts using MJ, liquid materials infused with metal nanoparticles should be used. In BJ technology (as shown in Figure 2.1(e)), a binder material in liquid state is selectively sprayed on

a thin layer of metal powder. This technology is among the fastest AM processes and requires no support structure. It also results in minimal distortions, such as warping or shrinking, in the printed parts and allows for flexibility in material selection. However, BJ could lead to final parts with poor material properties, and it is also generally less accurate than MJ technology.

As the name suggests, the SL process involves layer by layer stacking and lamination of thin sheets of metal material that are cut to the shape of the part's cross section using laser (as shown in Figure 2.1(f)). There are two groups of SL processes: Laminated Object Manufacturing (LOM) and Ultrasonic Additive Manufacturing (UAM). In LOM, which is primarily used for paper material but rarely for metal sheet, adhesives are used to bond the layers. Metallic parts printed using LOM are generally weak and not suitable for robust structural applications. On other hand, in UAM, an ultrasonic welding operation is used to bond the sheets. UAM also requires additional post-processing to remove excess unbounded material. Another major disadvantage of SL technology is its difficulty in printing geometrically complex parts. It also has low accuracy and poor surface finish. However, this technology benefits significantly from efficiency in manufacturing time and costs.
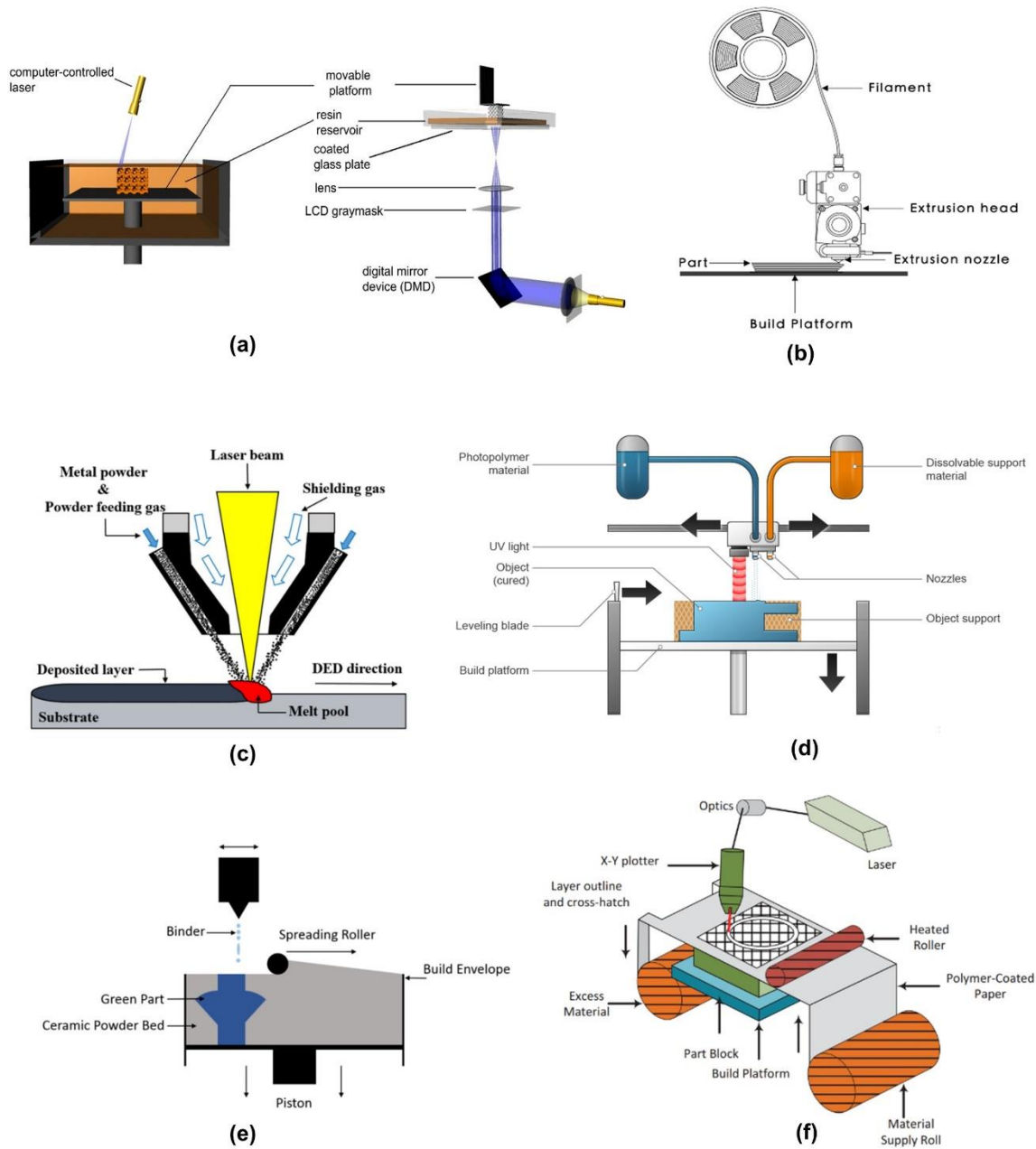
Figure 2.1: Schematic representation of six of the seven major metal AM categories: (a) VP [2], *(b) ME* [4], *(c) DED* [5], *(d) MJ* [6], *(e) BJ* [7], *(f) SL* [8].

2.2   LPBF Processes

In LPBF (see Figure 2.2), a layer of powder is deposited on the build platform, or the

substrate and the powder layer is flattened by a roller. Then, the heat or energy source, which

could be an electron or laser beam, is reflected through a scanning mirror and selectively melts

or sinters the powders. Finally, the substrate is lowered by the height of one layer thickness and

the process is successively repeated until the entire part is constructed. The unfused powder can

potentially be recycled and reused in subsequent prints. To avoid oxidation, the entire process

takes place inside a chamber with a shielding gas, such as Argon or Nitrogen. There are four

variations of LPBF technology which are very similar: Selective Laser Melting (SLM), Electron

Beam Melting (EBM), Direct Metal Laser Sintering (DMLS), and Direct Metal Laser Melting

(DMLM). In EBM, a beam of electrons is used to fully melt powders while in SLM, DMLS, and

DMLM laser is used to fuse metal powder together.

In LPBF processes, the characteristics of the powder as well as process parameters have a

significant effect on the quality and mechanical performance of the printed parts. There are over

one-hundred process parameters in most modern LPBF systems [9]. However, the major ones

include laser power, powder layer thickness, laser scanning velocity, hatch spacing (i.e., distance

between successive tracks), and scanning strategy. Powder layer thickness in LPBF processes

ranges from 20 to 100 µm, with powder particle sizes ranging from 20 to 45 µm [10]. Most

LPBF machine manufacturers develop sets of optimized process parameters for each powder

material to produce dense materials, minimize defects, improve surface finish, increase

efficiency, or produce parts with robust mechanical properties. Since it is not possible to agree

on a single set of process parameters that are fully optimized to produce the "perfect" part,

manufacturers develop general parameters to meet as many priorities and quality requirements as possible.
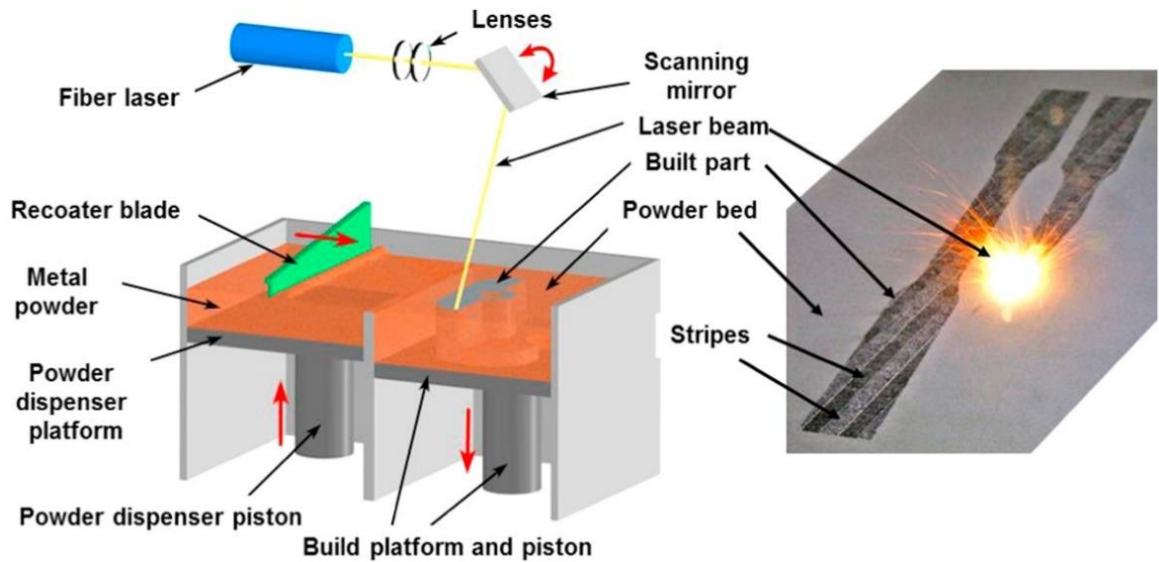
Figure 2.2: Graphical representation of the LPBF system adopted from [11]

2.2.1 LPBF Advantages

LPBF processes have numerous advantages which explains their prominence over other metal AM technologies in the market. In fact, LPBF processes have recently been used for manufacturing production parts as opposed to prototyping purposes only. This has resulted in adoption of this technology in producing parts for a variety of industries, including but not limited to medical, aerospace, and automobile. One of the major benefits of LPBF is that it allows for flexibility in printing highly complex geometries and metallic components, such as lightweight freeform structures or lattice structures.

Moreover, LPBF allows using a broad selection of powder materials and specifically high-strength super-alloys that are primarily used in aerospace applications and products. The range of metal powders that can be processed by LPBF is constantly growing and currently include titanium, aluminum, chromium-cobalt, nickel-based super alloys, and a variety of steels which

are commercially available in the powder form [10]. Additionally, LPBF offers significant

reduction in material waste and hence it is categorized among the most sustainable and efficient

AM technologies. However, LPBF has several major disadvantages and challenges that are

discussed in the next section.

2.2.2 LPBF Drawbacks and Defects

As discussed in Section 2.2.1, low cost, wide material choice, and low material waste are

the major advantages of LPBF over other metal AM technologies. However, there are several

major limitations associated with the process as well. Firstly, LPBF is a relatively slow AM

process with long build times that are due to the additional time required for preheating of

powder, recoating step, and cooling off period. Therefore, to increase the printing speed, many of

the recent LPBF machines utilize multiple lasers. However, addition of lasers increases machine

cost as well as complexity of the overall system.

Post processing and heat treatments, such as Hot Isostatic Pressing (HIPing) process, may

be required to improve the mechanical properties and metallurgical issues of the final LPBF

parts. The layering in AM processes often leaves a slightly "stepped" or rough surface finish

which requires post-processing by sanding or blowing to eliminate the roughness. During the

HIP heat treatment process, high temperatures and high pressures are applied in a HIP furnace

(pictured in Figure 2.3) to reduce the porosity while densifying the part.
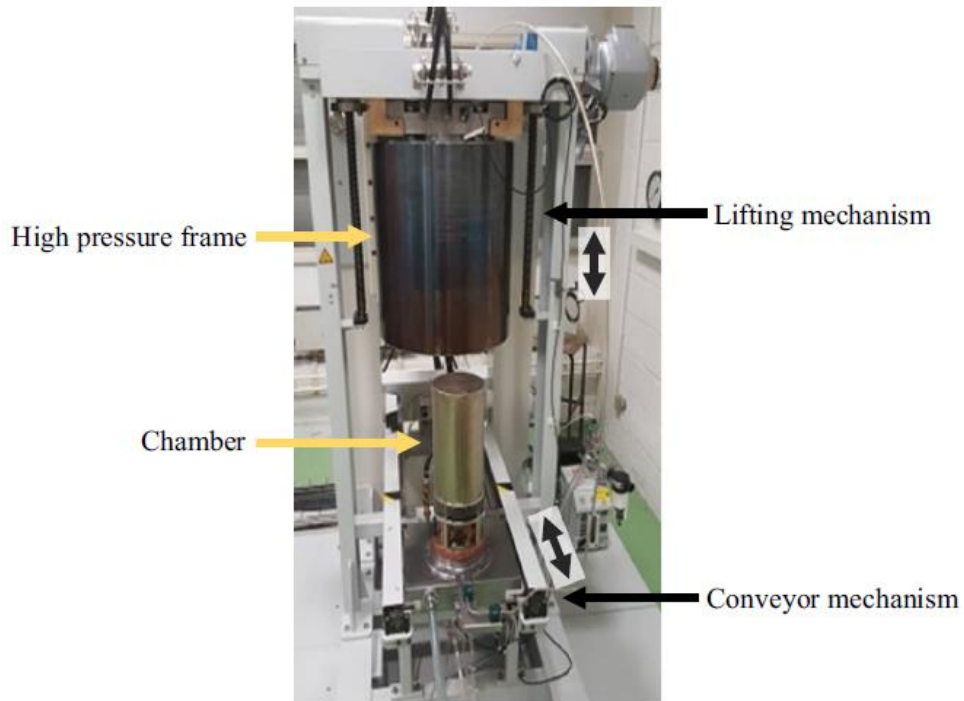
Figure 2.3: Schematic of a HIP furnace adopted from [12]

Despite the significant improvements in LPBF processes, there are several defects

generated during the process that can be divided into three major categories: microstructural

defects (such as porosity and undesired microstructure), surface quality defects (such as

roughness from instabilities and balling effect), and structural defects (such as residual stresses)

[13,14]. These defects are depicted in Figure 2.4. Formation of pores is commonly observed in

LPBF components and is categorized into three groups: lack-of-fusion pores, keyhole-induced

pores, and gas-induced pores. Lack-of-fusion pores occur due to incomplete melting as a result

of insufficient energy and are typically thin and irregular in shape[15]. On the other hand, high

energy input causes keyhole-induced pores as the metal vaporizes and a slender vapor cavity

(i.e., keyhole) becomes trapped. Lastly, small spherical gas-induced pores can occur due to

entrapment of shielding gas and vaporized elements during the LPBF process [16,17]. This is discussed in more detail in Section 3.1.7.

Another detrimental defect in LPBF processes is the balling phenomenon which happens due to the tendency of the melt-pool to shrink (or ball up) under the action of surface tension to reduce free energy. The balling effect could hinder the quality and performance of the printed object through increasing surface roughness as well as introducing pores into the micro-structure of the printed part. Due to the complex physical and chemical interactions between the laser and the powders, balling phenomenon is very complicated to model. The balling effect has been found to happen for two main reasons: formation of coarse balls due to inadequate laser energy input to cause melting of powders and formation of balls due to Rayleigh instability of the melt-pool under high scanning speeds. However, other factors, such as the contamination resulting in a layer of oxide that reduces surface energy of the substrate and causes poor wettability, are also crucial in causing the balling behavior [18]. In addition to the balling effect, melt-pool instabilities and spattering also can lead to low surface finish quality and high surface roughness during LPBF processes.

Lastly, one of the major drawbacks of metal AM technologies are residual stresses and thermal distortions. Residual stresses could lead to crack formation in the fabricated parts and are caused by the localized heat source that produces high thermal gradients. Undesired thermal stresses could cause failure both during and after printing the part [19]. It must also be mentioned that LPBF defects are interdependent such that if high surface roughness or porosity exist, the stress distribution could change and that could lead to local stress concentration which creates crack initiation sites. In short, lack of control of the temperature field during LPBF can lead to many of the aforementioned defects appearing in different scales in the printed parts. Therefore,

14

in order to minimize such defects, it is essential to understand, predict, and also control the temperature field during the printing process. Section 2.3 aims to thoroughly discuss the existing modeling approaches for LPBF processes and the associated advantages and disadvantages of these different methods.
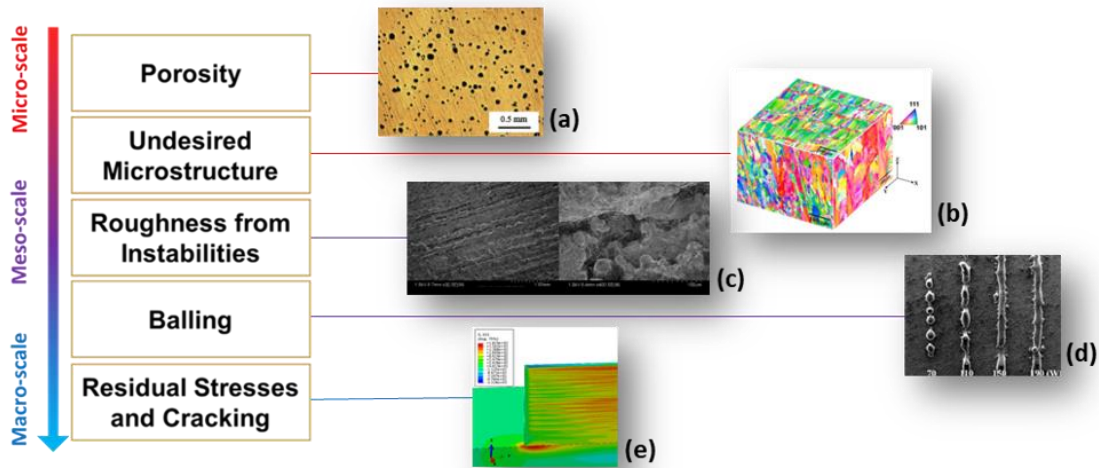
Figure 2.4: Major defects generated during LPBF processes: (a) [13]*, (b)* [14]*, (c)* [15]*, (d)* [18]*, (e)* [19]

2.3 Conventional Approaches in Numerical Modeling of LPBF Processes

LPBF processes have a chaotic nature that could easily lead to defects if process parameters are not chosen cautiously. The multi-scale AM process involves complex micro time and length scale physical phenomena (as pictured in Figure 2.5) , including spattering, laser absorption, diffusive and radiative heat conduction in the melt-pool and in the powder, evaporation, capillary effects, and many more. Therefore, accurate simulation of the LPBF process requires conducting sophisticated multi-scale multi-physics numerical modeling to predict defects and investigate the effect of process parameters on the final part.

15
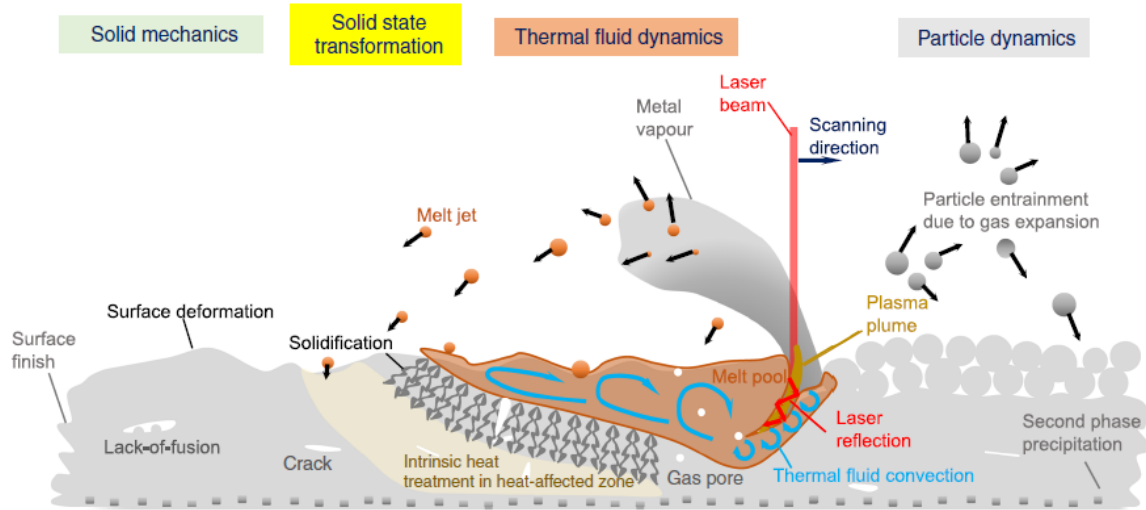
Figure 2.5: Schematic representation of physical phenomena happing during LPBF at different length and time scales adopted from [20]

There are two main categories of thermal modeling approaches for LPBF processes. The first group, discussed in Section 2.3.1, is based on simplified conduction-only thermal models that neglect fluid flow effects and perform Finite Element Analysis (FEA) on a continuum domain with effective powder properties. And the second group, discussed in Section 2.3.2, is based on high-fidelity yet computationally intensive thermo-fluid simulations that account for fluid flow effects and specifically the convection in the melt-pool for small-scale simulations. In order to mitigate or control residual stresses and consequent part distortion, it is essential to link the transient temperature field to thermal strains and investigate the thermo-mechanical behavior of parts during printing.

The existing coupled thermo-mechanical models have been reviewed and presented in Section 2.3.3. The existing approaches in modeling the microstructure evolution have also been discussed in Section 2.3.4. Specific aspects of a numerical model of the LPBF process, such as heat source modeling, heat absorption modeling, and definition of material properties for powder and bulk material have also been reviewed in Sections 2.3.5, 2.3.6, and 2.3.7, respectively.

16

In addition to numerical models, a literature review has also been carried out in Section 2.3.8 to identify the state-of-the-art data-driven and physics-informed reduced-order models for AM processes. Data-driven reduced-order models are based on machine learning approaches involving training based on a set of data, which are either extracted from physics-based simulations or obtained from experimental measurements and has the potential to be used for near-real-time prediction and AI-assisted defect control for the AM process. Lastly, Section 2.3.9 reviews some of the existing commercially available software that have been specifically developed for modeling metal AM processes.

2.3.1 Conduction-only Thermal Models

A significant number of existing thermal simulations assume a continuum domain with effective powder properties and have utilized FEA to investigate temperature field evolution during the LPBF process. Multiple critical review papers discuss existing conduction-only thermal models for LPBF processes [21,22]. In the earlier days, most of such simulations were focused on heat conduction models for single-track LPBF processes only [23,24]. To increase practicality of these models for actual LPBF processes, conduction-only heat transfer models were then extended to multi-track [25,26] and multi-layer [27] simulations.

Figure 2.6(a) presents thermal field predictions obtained by Hu *et al.* from 3D FEA using ANSYS for five-layer deposition of AlSi10Mg alloy during LPBF process. Due to their efficiency in structural level modeling, conduction-only thermal models have been predominantly used in coupled thermo-mechanical analysis for the LPBF process. However, these simplified thermal models characterize physical phenomena at the macro scale and neglect melt-pool dynamics which leads to inaccurate predictions of the temperature field.

2.3.2 *Thermo-fluid Models*

Fluid flow has been ignored in the vast majority of existing thermal modeling studies for LPBF processes, but several recent numerical models coupled heat transfer with fluid flow for single-layer simulations. These micro-scale models incorporate effects of Marangoni convection and other interfacial phenomena to increase the accuracy of the predictions as well as the computational cost of the simulations. To avoid additional computational load, some CFD simulations assume a flat and rigid liquid-gas interface and hence do not resolve dynamic interfacial fluctuations [28]. On the other hand, other models track the liquid-gas interface using the Volume of Fluid surface-tracking method [29], Level Set method [30], a combined approach [31], or other interface-tracking methods. From interface-tracking CFD simulations, it is also possible to predict and study process-induced micro-void formation and their dispersion parameters, such as volume fraction, size and shape for single-track LPBF [32].

Additionally, high-fidelity thermo-fluid models can be used with or without powder packing simulations such as Discrete Element Methods [33]. The majority of the existing CFD simulations are for fundamentally homogeneous models and hence to break away from this homogeneity, powder-packing simulations were developed. By considering geometry, size, and distribution of powder particles, these models make the powder bed behave non-uniformly and account for the granularity of the process. Therefore, these fine-scale models would give realistic results while being more computationally demanding compared to thermo-fluid models without powder packing.

Due to the intensive computational costs, there exists very few multi-track yet multi-layer CFD simulations in literature [34,35]. In other words, the convection of liquid metal in the melt-pool during LPBF is often neglected in multi-track and multi-layer simulations. Figure 2.6(b)

18

represents results of a transient thermo-fluid simulation for multi-layer LPBF process by Mukherjee *et al.* [35]. Although they successfully used a traveling grid system to increase efficiency, multiple simplifying assumptions, such as temperature-independent material properties and neglecting heat loss due to vaporization, had to be made to maintain reasonable computational costs.

An alternative to modeling fluid dynamics is incorporating fluid flow effects numerically in conduction heat transfer models rather than explicitly modeling fluid flow and solving the governing equations, i.e., the Navier Stokes equations, at the micro scale. Examples of such implementations are incorporating evaporation through a heat sink on the surface of the powder bed as proposed by Karayagiz *et al.* [36], and accounting for Marangoni convection effects through increasing thermal conductivity of the liquid phase by a reported factor [37,38]. In Chapter 3, a thorough description of these techniques and their implementation in the proposed modeling approach will be provided.

In addition to coupling the thermal field with a mechanical model to study the development of residual stresses, it is also possible to feed the thermal model into a microstructure simulation to predict grain growth and microstructure evolution during the solidification process. Li *et al.* [39] recently published a review paper discussing the four conventional methods (i.e., Cellular Automata, Phase Field, Monte Carlo, and deterministic methods) used in the microstructural simulation of the solidification process for Ti-6Al-4V during LPBF.
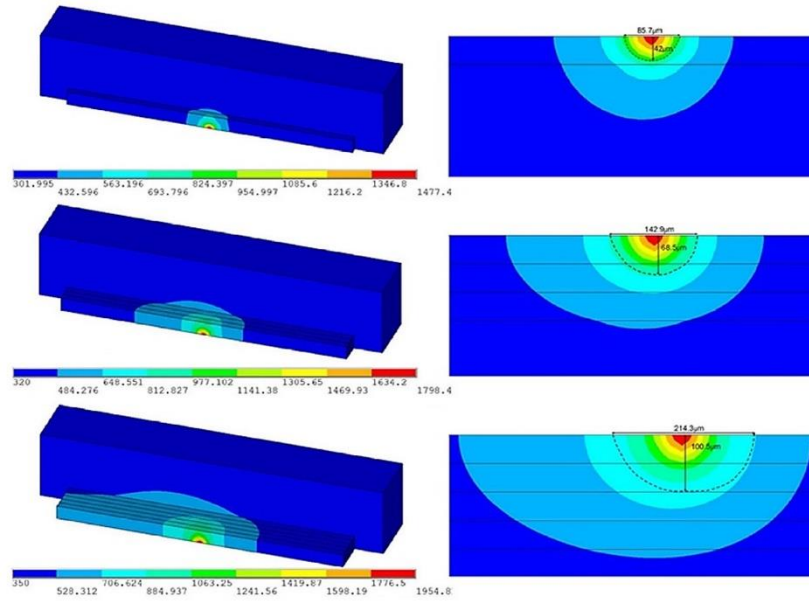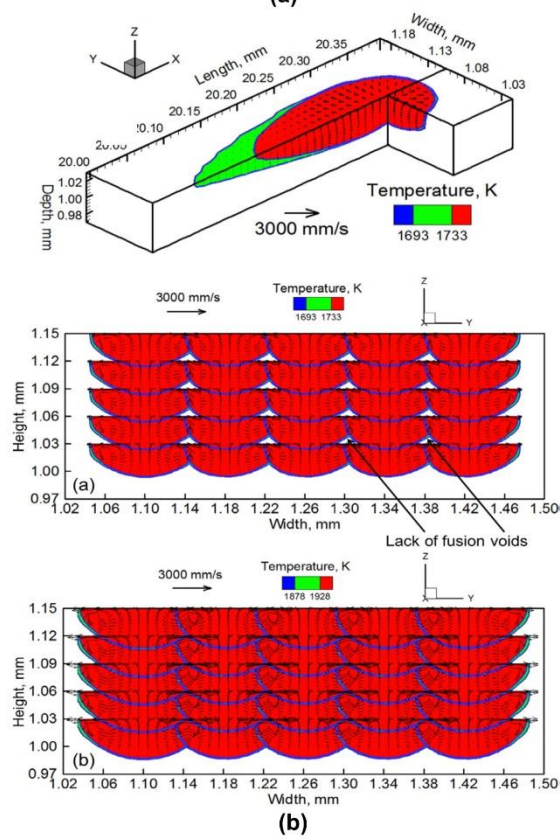
Figure 2.6: Thermal field results from (a) conduction-only model by Hu et al. [27], *(b) thermo-fluid CFD simulation by Mukherjee et al.* [35].

2.3.3 *Thermo-mechanical Models*

A pre-requisite for producing high quality LPBF products is predicting and controlling thermal stresses and associated distortions during the printing process. Post-AM residual stress measurements although widely conducted, could be too late to save a product from failure once a defect appears. On the other hand, in-situ residual stress measurement faces many challenges such as extremely high temperatures and spatters that are generated during most laser-based AM processes and affect positioning of measurement systems. Therefore, FEA has gradually become a powerful tool for studying thermal stresses during the LPBF process. However, it is also worth mentioning that recently, new methods have been developed to combine experimental data and computer vision with FEA to monitor stress evolution during AM processes [40]. Due to its ability in handling highly non-linear problems, FEA is identified as the preferred numerical method to study the thermo-mechanical behavior during the SLM process.

Numerous research has been conducted to study residual stress and part distortion during LPBF processes using commercially available FEA software, such as Abaqus [41,42], ANSYS [43] and COMSOL Multiphysics [44]. These sequentially coupled thermo-mechanical numerical models link transient temperature fields to thermal strains. Conventionally, the transient temperature field can either come from a conduction-based heat transfer model or a thermo-fluid CFD simulation. Because of their efficiency in part-scale modeling, most multi-layer thermo-mechanical models of LPBF processes are based on macroscale conduction-based thermal models. An example is the sequentially coupled FEA thermo-mechanical model developed by Cheng *et al.* [41] in Abaqus. Although computationally efficient, their model is missing effects of convection of liquid in the melt-pool which has a huge impact on the predicted stress fields.

The residual stress predictions in X-direction of several different scanning strategies are presented in Figure 5(a).

Chen and Yan [45] coupled an interface-tracking thermo-fluidic model that includes powder packing with a mechanical model, CFD-FEM, to study thermal stresses and distortions during LPBF. However, due to high computational costs, their model is limited to two tracks and two layers only. The thermal stresses predicted by their CFD-FEM model are presented in Figure 2.7(b). Another example is the Abaqus-based thermo-mechanical model, with temperature field coming from a thermo-fluid model, by Mukherjee *et al.* [42]. They were able to model 10-layer depositions of IN718 and Ti-6Al-4V powder layers. However, as explained earlier in Section 2.3.2, several major simplifying assumptions had to be made to keep their approach efficient while affecting the accuracy of the predictions.
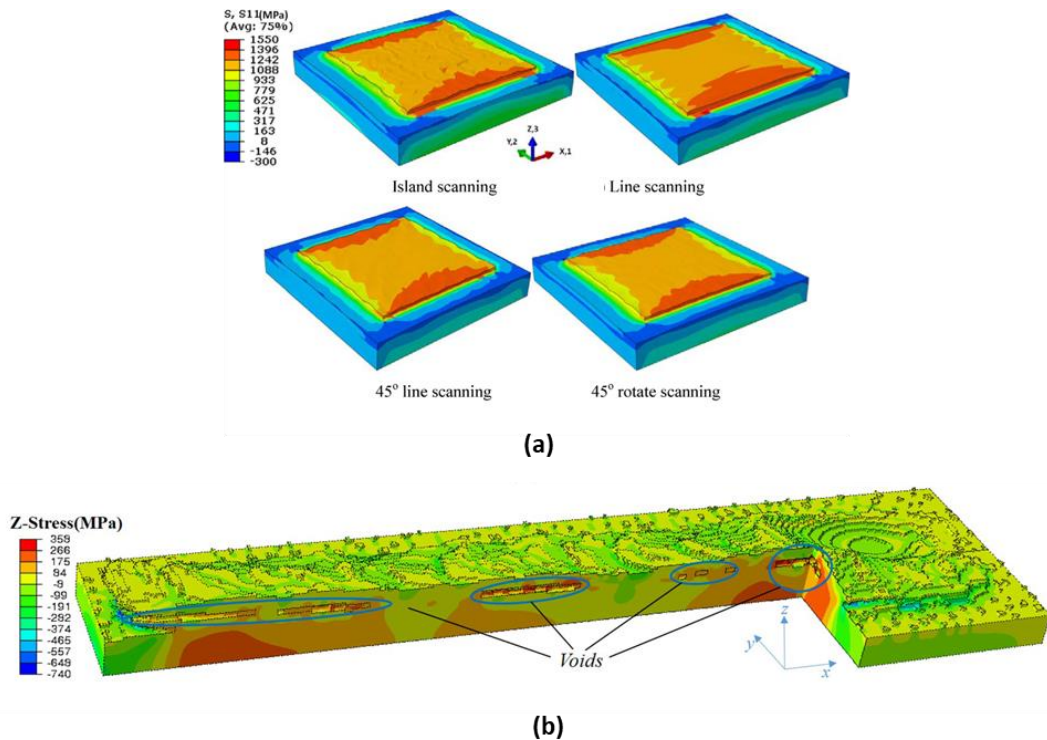
Figure 2.7: Predicted thermal stresses with thermal field coming from (a) a conduction-based thermal model by Cheng et al. [41]*, (b) a thermo-fluid CFD simulation by Chen and Yan* [45]*.*

22

2.3.4 Microstructure Modeling

Predicting the microstructural evolution during metal AM processes is critical and hence has been extensively studied in literature. Microstructure modeling helps with adjusting process parameters to achieve desired microstructures and hence mechanical properties. In a recent review paper, Korner *et al.* [46] discuss the four conventional modeling approaches (i.e. Phase Field model, Cellular Automaton, and Monte Carlo method) used in the microstructural simulation of the solidification process in metal AM processes.

The basis for microstructure modeling is the thermal field. In other words, the temperature field is fed into microstructure simulations to predict grain growth and microstructure evolution during the solidification process. The Phase Field (PF) model can be used to solve complex interfacial problems of micro length scale. However, due to its high computational costs, the mathematical PF model is usually restricted to very small regions. There are several open-source tools, such as the PRISMS-PF framework [47] (developed by the PRISMS Center) which uses an efficient matrix-free FE approach and MOOSE-PF [48] (developed by the Idaho National Laboratory) that can be used to develop and employ PF models.

Cellular Automaton (CA) is another approach that is commonly used to model grain structure evolution during metal AM processes. For instance, Lawrence Livermore National Lab has recently published an open-source source code on github, called the Exascale CA (ExaCA) built upon the Kokkos library [49]. ExaCA is specifically useful when modeling AM processes as it utilizes a parallel-in-time approach to address the sequential nature of scanning in AM processes and avoid high computational costs by simulating one layer at a time. Unlike PF and CA methods, the Monte Carlo (MC) method uses random numbers and probability for grain grown simulation. MC method is a relatively simple and efficient method that is proved to be

effective in simulating grain growth behavior [39]. For instance, Sandia National Laboratories has developed a kinetic MC source code, called SPPARKS, that is readily available on github and can be used for microstructural evolution simulations [50]. It is also worth noting that there are commercial software packages that use a combination of these methods to tackle microstructure simulations. For instance, PhasePot integrates the PF in combination with MC models to simulate the microstructure evolution [51].

2.3.5 Heat Source Modeling

One of the most important aspects of thermal and thermo-fluid modeling of LPBF processes is the definition of the moving heat source. Heat source can be modeled as a point source, 2D flux, or 3D power distributed over a volume. In 1946, Rosenthal [52] developed an exact analytical solution for heat conduction equations with one-dimensional (i.e., point) moving heat source on the surface of a semi-infinite metallic plate. Later in 1983, Eager and Tsai [53] introduced a two-dimensional moving heat source with Gaussian-distributed power to predict the weld geometry.

In 1984, this was upgraded to a three-dimensional double-ellipsoidal moving heat source by Goldak *et al.* [54] to increase the accuracy of the predictions. However, the use of 2D heat sources have been more common in LPBF simulations due to their simplicity and proven to be sufficient in thermal models for LPBF processes. Another common type of heat source model adopted in literature is the Ray Tracing model [55] which is uncommon due to the lack of available information for estimation of the penetration depth and proper definition of the heat source .

2.3.6 Heat Absorption Modeling

In LPBF processes, the net amount of energy absorbed by the powder bed depends on many factors, including the characteristics of the energy source such as laser wavelength as well as the characteristics of the materials such as inter-reflection of the laser beam among powder particles [56]. Therefore, the reported value for each material varies widely in literature. To tackle such challenges, many efforts have been made to utilize analytical and experimental studies in approximating the absorption of laser light by the metal powder. For instance, Promoppatum *et al.* [57] conducted numerical studies, using reported data on absorptivity of IN718 in literature, to determine the fitted absorptivity that gives the closest estimate of measured melt-pool width for a laser wavelength of $1.06 \ \mu m$.

Although most modeling approaches assume a constant absorptivity as a common approximation, it must be mentioned that incorporating a material and process dependent absorptivity helps with achieving melt-pool sizes that align better with experimental measurements. An example of such approach is utilizing scaling laws, as defined by Gan *et al.* [58], that can also facilitate process optimization and defect elimination in LPBF processes. Details about this approach are described in Section 3.1.2.

2.3.7 *Thermo-physical and Mechanical Properties*

Thermo-physical properties, i.e. thermal conductivity, density, and specific heat capacity, of alloys vary significantly with temperature. Therefore, the assumption of constant thermo-physical properties could reduce the simulation accuracy. The majority of the existing thermal models for LPBF processes incorporate temperature-dependent thermo-physical properties [25,28,31] while a few of them assume constant values [59]. Additionally, the majority of thermo-mechanical simulations have used temperature-dependent mechanical properties, i.e.

Young's modulus, thermal expansion coefficient, and yield stress, for more accurate predictions [19,42].

Since the powder domain is modeled as continuum homogenous material, incorporating effective properties for powder is essential. The effective thermo-physical properties of the powder bed could be dependent on the packing density of the powder bed, properties of the shielding gas entrapped among the powder particles, and bulk material properties [60]. The numerical treatment of latent heat effects is commonly implemented using two schemes, the simple Apparent Heat Capacity method and the more involved Heat Integration method. Proell *et al.* [61] also proposed a variant of the heat integration scheme that allows for higher efficiency and accuracy through a user-defined tolerance.

2.3.8 *Reduced-order Modeling*

In addition to numerical simulations and experimental measurements, Reduced Order Modeling (ROM) has become a very attractive predictive tool in recent years. ROM is referred to a model based on Machine Learning (ML) or Deep Learning (DL) of data obtained from experimental measurements or physics-based simulations. The goal of such ROMs is to discover the relationship between a set of available input data and to predict outputs even if there is no phenomenological understanding [60]. There are multiple critical review papers on ROM approaches in AM [62,63]. Most current approaches use datasets stemming from experimental measurements [64,65], numerical simulations [66,67], or a combination of both [68]. In this dissertation, ROMs based on experimental measurements are referred to as *black-box* models, ROMs based on solutions of numerical simulations are referred to as *grey-box* models, and *white-box* models are those based on physics-based simulations.

26

Multi-scale multi-physics white-box models are accurate yet very computationally expensive and complex in modeling LPBF processes. Therefore, for real-time applications, such models are often not appropriate. On the other hand, black-box models are efficient and suitable for real-time control systems. However, they are costly, time-consuming to develop, and majorly lack interpretability. Therefore, grey-box models are more suitable for real-time applications, including digital twins. A successful grey-box model benefits from large amounts of data. Producing a database to help develop a grey-box model can be prohibitively expensive. However, it still offers many advantages, including flexibility in modeling for different materials and process parameters without the time, cost, and manpower required to run numerous experiments [69].

There are limited available grey-box models, supervised or unsupervised ML, applied to AM processes. In their review paper, Qi *et al.* [62] identified Neural Networks (NN) to be the prevalent ML method applied to different aspects of AM due to its ability of discovering complicated patterns. Mozaffar *et al.* [66] used Recurrent Neural Networks (RNN) trained by data obtained from an in-house FE code, GAMMA, to predict the thermal histories during the Direct Energy Deposition (DED) process. Similarly, Paul *et al.* [66] presented a novel framework that uses data from GAMMA, an in-house FE code, to train a ML model with extremely randomized trees. Many researchers also developed prediction grey-box models based on Convolutional Neural Networks (CNN). Khadilkar *et al.* [70] developed a CNN-based model from FE simulations to predict stresses during Stereolithography (SLA) printing process. Wang *et al.* [71] also trained a NN to quickly predict separation stress distribution during the pull-up process in SLA using FE simulation data from Abaqus.

27

Most recently, Sofi and Ravani [72] have developed an encoder-decoder CNN to obtain sub-second predictions of the heatmap for different scanning strategies during single-layer selective laser sintering, which can be further developed for close loop control system for AM digitalization. Although utilizing ML approaches would enable fast predictions of temperature and stress fields during AM processes, there are challenges associated with these techniques (such as large amount of accessible data, proper selection of the significant process parameters as inputs to the network, etc.) that need to be considered when training ML models.

Training and constructing ROMs could be timely and/or costly, depending on the nature of the data gathering process. Therefore, to reduce the costs associated with gathering simulation data, physical knowledge can be incorporated into developing ROMs. The loss functions of physics-informed ROMs can be constructed based on governing Partial Differential Equations (PDEs) [73]. A relevant example is the work of Zhao *et al.* [74] in which a physics-informed CNN model is trained to simulate the thermal field during LPBF using a static heating source on a 2D plane.

ROMs, in general, allow for near-real-time predictions and hence could potentially be used as an engine in developing a digital twin for the AM process. A digital twin is a digital model of a real-life object, process, or system. Rather than a virtual model in isolation, a digital twin is constructed in such a way to exchange real-time information with its physical counterpart [75]. In other words, the virtual representation is continuously being updated with real-time data. Although digital twins of products, such as jet engines, power turbines, and vehicles, have existed for some time, digital twins of processes are relatively new. The objective of a digital twin for AM processes is to reduce the total number of experiments needed for quality assurance of printed parts, i.e. to minimize defects and produce structurally reliable parts [76].

2.3.9 *Commercially Available Software Packages for Modeling Metal AM Processes*

More recently, advanced simulation tools have been developed to help the AM community tackle modeling challenges and difficulties more easily. However, before reviewing some of the existing well-known commercially available AM software packages, it must be mentioned that there are many challenges in using these software packages for practical applications and specifically for developing digital twins of AM processes. The most significant challenge is the high computational cost and power requirement for running such simulations as well as costly license access for most of the packages. However, it must be mentioned that a few of these new tools offer reduced computational times and less complexity in modeling AM processes. Some recent studies have surveyed several of these computational tools and compared their capabilities of simulating AM processes [77]. Some of these AM simulation tools include ANSYS Additive Print [78], Atlas 3D Sunata [79], Amphyon [80], Simufact Additive [81], Autodesk Netfabb [82], and FLOW-3D AM [83].

ANSYS Additive Print is a software package that offers different levels of simulation fidelity for thermal and stress analysis during metal AM processes. Some of the major capabilities of the software include predicting distortions and automatic distortion compensation as well as predicting in-process stresses and final residual stresses using the inherent strain method. This stand-alone AM simulation tool allows users and designers of metal AM parts to introduce appropriate countermeasures at an early stage and avoid time-consuming design considerations.

Released in 2018, Atlas 3D Sunata is a cloud-based software that offers a more computationally efficient approach by performing thermal analysis using the Thermal Circuit Network (TCN) model as opposed to conventional FEM. In the TCN method, the build process

29

is segmented into smaller groups that are then connected like nodes to enhance efficiency in thermal modeling of the layer-by-layer process. Sunata also offers optimizations depending on the users' priorities of minimizing build time, distortion, support removal, etc. A unique feature of this software is enabling users to optimize the build tray when printing a collective of geometries while ensuring no thermal cross contamination takes place. Similar to Additive Print, Sunata offers distortion compensation to guarantee the printed part matches closely with the input STL file.

Another commonly used tool is Amphyon which is also a standalone software tool used by designers and engineers for modeling metal AM processes. Amphyson also utilizes the inherent strain method for predicting residual stresses and thermal strains. The modular software package offers different modules including pre-deformation module, supports module, examiner module, mechanical process simulation module, thermal process simulation module, and thermal adaptation module. The modules are constantly being developed to increase the usability of the software in practical applications. Similar to Additive Print and Sunata, Amphyon also offers distortion compensation by the pre-deformation method in which the distortions are projected in an adverted way back to the CAD file.

Simufact Additive can also be used to model metal-based AM processes, namely LPBF and BJ processes. Simufact is a multi-physics simulation tool that can be used to predict stresses, temperatures, and distortions throughout the printing, heat treatment (e.g., HIP process), and machining processes, i.e., before the part is actually printed. Moreover, the software offers a comprehensive material database for most commonly used metal AM materials.

Autodesk Netfabb is another AM software tool that offers capabilities including but not limited to preparing and simulating AM processes. The software is aimed to help with scaling the

workflow and streamlining the day-to-day work of printing parts. A unique feature of Netfabb is topology optimization which enables the designers and engineers to apply AM features to the desired parts and design for the required load and weight conditions.

Unlike previous software that were aimed for part-scale modeling, FLOW-3D is a commercial CFD software that simulates at the micro- and meso-scales. And, FLOW-3D AM is specifically developed to model LPBF processes and can be used as a high-fidelity simulation tool to model the end-to-end process, from powder spreading to powder melting. FLOW-3D AM is a combination of two separate software packages: FLOW-3D DEM which can be used to model the particle-particle interactions in powder bed formation process and FLOW-3D WELD which can be used to model laser-material interaction for a variety of applications such as laser welding, laser cladding, DED processes, etc. The sequence of model set up using FLOW-3D AM is as follows: powder spreading using FLOW-3D DEM, laser irradiation using FLOW-3D WELD, and looping through the prior steps for multi-layer builds. High-fidelity FLOW-3D AM can accurately characterize the melt-pool dynamics and predict the onset of balling effect and porosity as well as surface morphology and microstructure evolution.

Chapter 3.   Development of the Simplified Multi-scale Modeling

(SMM) Approach

The proposed physics-based SMM, as illustrated in Figure 3.1, allows for considering lower length scale physics in modeling the thermo-mechanical response of alloys during multi-layer LPBF processes. The major component of the SMM approach is CTM which aims to link high-fidelity micro-scale and macroscopic simulations. In other words, it aims to serve as a more efficient alternative for computationally expensive high-fidelity CFD simulations and a more accurate alternative for over-simplified conduction thermal models used for modeling of the multi-layer deposition process.

In order to maintain the efficiency of the multi-layer CTM, volume shrinkage due to melting as well as mass loss due to evaporation are neglected. Section 3.1 describes the features of the CTM and Section 3.2 aims to cover the coupling between the thermal model and the mechanical model in simulating the stress state for multi-layer LPBF process. Also, Section 3.3 aims to discuss how the presented model can be utilized for developing data-driven and physics-informed ROMs.
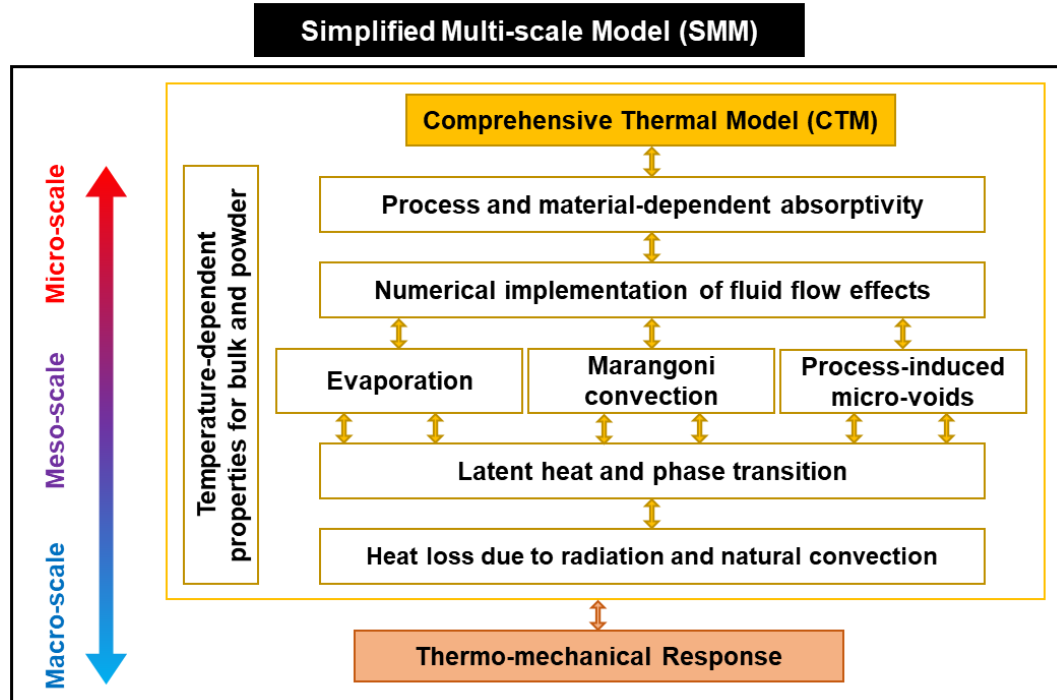
Figure 3.1: A schematic representation of SMM approach and the major components of the CTM

3.1 Comprehensive Thermal Model (CTM)

The distinct features of CTM are outlined in Figure 3.1. The figure aims to represent major micro, meso, and macro level physics that are accounted for in multi-scale modeling of the LPBF process. The foundation of the physics-based CTM is conduction with additional features including process and material dependent absorptivity, evaporation, Marangoni convection, process-induced micro-voids, latent heat, and phase transition effects as well as thermo-physical properties for bulk and powder material. The objective of the CTM is to obtain more accurate temperature predictions than simplified conduction-only models and higher efficiency than high-fidelity CFD simulations. It must also be mentioned that the model can conveniently be expanded to a wide range of alloys provided sufficient information is available. The CTM is implemented using the *Heat Transfer Module* in COMSOL Multiphysics® with MATLAB [84] as a scripting tool to automate and parameterize the simulation process for multi-layer deposition

33

across different alloys. The simulation domain, as depicted in Figure 3.2, consists of $1\ mm \times 1\ mm \times 30\ \mu m$ powder layers and a substrate, of the same material, with the dimensions of $2\ mm \times\ 2\ mm \times 0.5\ mm$.
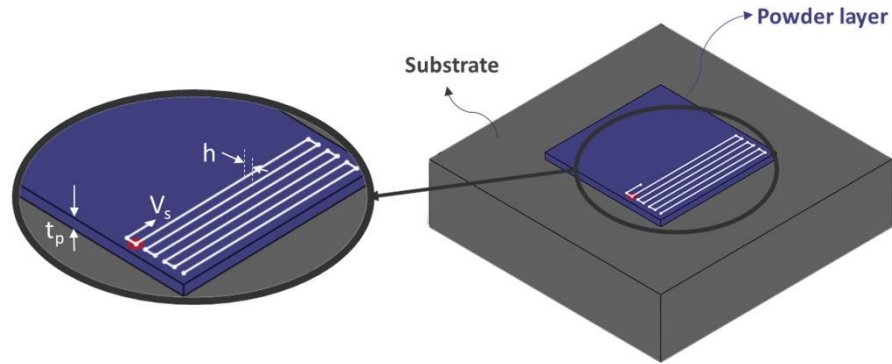
Figure 3.2: 3D model of the simulation domain and the scanning strategy

As the laser passes over the powder layer, for the first few layers, heat dissipates through and hence the melted material attaches to the substrate. As a result, if the substrate and the powder are of dissimilar materials, mixing of the two materials would take place during the scanning of the first few layers. This effect could significantly change the surface tension gradients and hence the Marangoni flow. Therefore, for simplification, in this dissertation, it is assumed that the powder and the substrate are of the same material. However, it is worth mentioning that in order to avoid unwanted mixing of alloys in LPBF processes, the experimentalists sometimes print inverted "feet" or pyramids (illustrated in Figure 3.3) for the first few layers and cut them off of the printed part after fabrication.
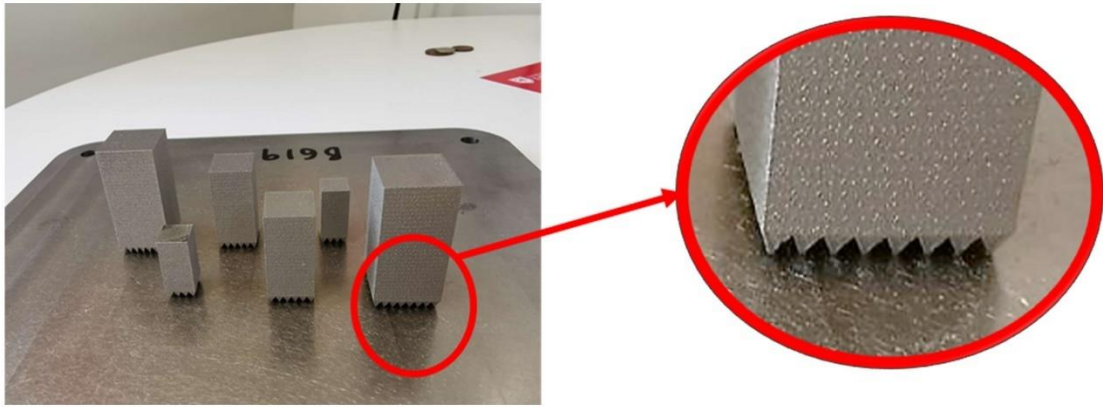
Figure 3.3: A series of printed parts with inverted "feet" or pyramids at the bottom. Courtesy of Yuanbo Tang from University of Oxford.

After a mesh independence study was carried out, it was determined that an 8-node hex mesh of size 25 μm is suitable for the powder region with coarser mesh for the substrate. For a 5-layer deposition simulation, the total computational time of the CTM ranged from 5 to 7 hours on a laptop with an Intel ® Core ™ i9-9880H CPU @ 2.30 GHz, 32 GB RAM. To put this into perspective, according to Strayer *et al.* [85], a high-fidelity CFD simulation for a 1 mm long track of IN718 took around 7 hours on 24 cores of the Intel Xeon Platinum 8268 @2.90GHz processor. This clearly indicates that the proposed CTM reduces the computational expenses significantly. As part of this research work, thermal history signatures, cooling rates, and melt-pool sizes across different alloys are computed and the results of the material-dependence study are presented and discussed in later sections.

3.1.1 Heat Conduction Model

As mentioned earlier, the CTM is conduction-based. Therefore, the governing equation for the heat transfer problem is the transient energy equation as presented below:

$$\rho(T)c_p(T)\frac{\partial T(\boldsymbol{x},t)}{\partial t} = k(T)\nabla^2 T(\boldsymbol{x},t) + q_{laser} \tag{1}$$

where $\rho(T)$ is the density of the material, $c_p(T)$ is specific heat, $k(T)$ is thermal conductivity, $T(\boldsymbol{x},t)$ is temperature, and q_{laser} is the heat source term. $k(T)\nabla^2 T(\boldsymbol{x},t)$ is the heat flux term governed by Fourier's law for an isotropic material where $\boldsymbol{x} = (x,y,z)$ refers to the position vector. Given appropriate initial and boundary conditions, the heat equation can be solved. In this model, the initial temperature of the entire domain, i.e., the powder bed and the substrate, is set at room temperature (T_0). Moving laser beam heat flux, natural convection (i.e., heat loss to the surroundings due to shielding gas flow), and radiation to surroundings are the thermal boundary conditions in this heat transfer problem:

$$T(\boldsymbol{x},0) = T_0$$
$$q_{radiation} = \varepsilon\sigma_B(T_0{}^4 - T^4) \tag{2}$$
$$q_{convection} = h(T_0 - T)$$

where ε is emissivity, σ_B is the Boltzmann's constant $(= 5.67 \times 10^{-8}\,{}^W\!/_{m^2 K^4})$, and h is the convective heat transfer coefficient. It must be mentioned that the proposed CTM assumes constant (i.e. independent of temperature) emissivity and heat transfer coefficient. One of the most important aspects of the thermal model for LPBF processes is heat source modeling of the laser beam. As discussed in Section 2.3.5, a surface heat source is accurate enough to model LPBF processes and hence is acceptable to use in the proposed CTM. The heat input is described by a Gaussian distribution as a function of distance from its center. In other words, such heat fluxes follow an axisymmetric Gaussian profile presented as follows:

$$q_{laser} = \frac{2AP}{\pi\omega^2}\exp\left\{-2\frac{[x - x_l(t)]^2 + [y - y_l(t)]^2}{\omega^2}\right\} \tag{3}$$

36

where A is absorptivity (as described in Section 3.1.2), P is laser power, $x_l(t)$ and $y_l(t)$ indicate position of the laser beam, and ω is laser beam radius.

3.1.2 Process and Material Dependent Absorptivity

Another important aspect of thermal modeling of LPBF processes is absorption of laser energy by the metallic powder and bulk material. As discussed in Section 2.3.6, absorptivity in LPBF processes is significantly affected by different factors that include the characteristics of the energy sources as well as the materials [60]. Therefore, accounting for process and material dependent absorptivity is critical in thermal modeling of LPBF processes. Proper definition of absorptivity is specifically important at higher energy inputs where keyhole mode is the major form of melting. For the proposed CTM, the absorptivity used is a function of both process parameters as well as thermo-physical properties as defined by Gan *et al.* [58] through scaling laws as following:

$$A = 0.7[1 - \exp{(-0.6 Ke_m L_d^*)}]$$

$$Ke_m L_d^* = \frac{A_m P}{(T_m - T_0)\pi \rho(T) C_p(T) V_s \omega^2}$$

(4)

where $Ke_m L_d^*$ is the scaling parameter, A_m is minimum absorptivity (i.e., absorptivity on a flat surface which is a material dependent property), and V_s is the laser speed. The scaling laws are developed based on in-situ synchrotron X-ray imaging data and high-fidelity multi-physics models for different materials and process parameters. In their experimental set-up, Gan *et al.* used 1070 nm for laser wavelength with maximum power of 540 W.

3.1.3 Latent Heat and Phase Transition

Latent heat and phase transition effects are among the most critical aspects of thermal modeling for LPBF processes. Phase variables, $\theta_i(T)$, keep track of volume fraction of solid

phase ($i = 1$) and liquid phase ($i = 2$) at every time-step and location in the simulation domain. For simplicity, the model does not explicitly track the gaseous phase. Tracking $\theta_i(T)$, which is depicted in Figure 3.4 for IN718, allows for utilizing temperature- and phase-dependent material parameters in phase transition regions.
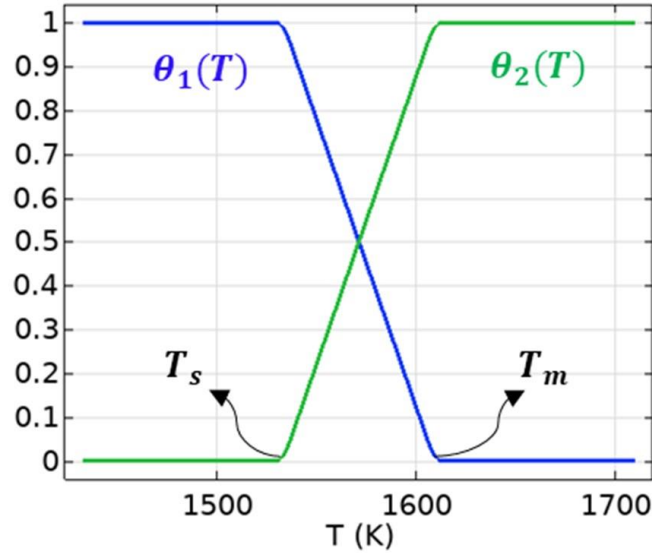
Figure 3.4:Plots corresponding to phase variables $\theta_i(T)$

The values of density and thermal conductivity during phase transitions are described by following equations:

$$\rho(T) = \theta_1(T)\rho_1(T) + \theta_2(T)\rho_2(T)$$

$$k(T) = \theta_1(T)k_1(T) + \theta_2(T)k_2(T) \tag{5}$$

$$\theta_1(T) + \theta_2(T) = 1$$

Using mixture relations and phase variables in defining properties through phase transition has commonly been used in previous studies such as the heat transfer model developed by Karayagiz *et al.* [36]. Also, in the present model, the Apparent Heat Capacity method is used to account for the latent heat of fusion in solid-to-liquid phase change [61]. In this method, the

specific heat capacity of the alloy is increased in its melting region (i.e., between solidus and liquidus temperatures) to account for the excess energy required in heating the material:

$$C_p(T) = \theta_1(T)C_{p,1}(T) + \theta_2(T)C_{p,2}(T) + L_f \frac{df}{dT} \tag{6}$$

where $f(T)$ is a smooth phase transition function and L_f is the latent heat of fusion. Additionally, in the CTM, temperature-dependent thermo-physical properties for powder and bulk material are used which are discussed in detail in Section 3.1.4.

3.1.4 Thermo-physical Properties

As mentioned in Section 2.3.7, utilizing effective thermo-physical properties for the continuum domain of the powder is critical. Although powder-scale approaches result in a more realistic simulation compared to continuum-scale simulations, such models could instantly become computationally expensive and hence impractical for part-scale simulations [36]. In the current modeling approach, the effective thermal conductivity and density of the powder are used as defined by Yin *et al.*[26]:

$$\rho_{powder}(T) = \rho_{bulk}(T)(1 - \varnothing(T))$$

$$k_{powder}(T) = k_{bulk}(T)(1 - \varnothing(T))^4 \tag{7}$$

where $\varnothing(T)$ is the porosity function defined as follows:

$$\varnothing(T) = \begin{cases} \varnothing_0, & T_0 < T < T_s \\ \varnothing_0 \left(\dfrac{T - T_m}{T_s - T_m}\right), & T_s < T < T_m \\ 0, & T_m < T \end{cases} \tag{8}$$

where $\varnothing_0$ is the initial powder porosity, T_s is the solidus temperature, and T_m is the melting temperature of the alloy. Initially, i.e., before the laser starts scanning, powder properties are assigned. As the laser scans and the molten material cools down and solidifies, bulk properties

need to be assigned. Therefore, to account for the transition from powder to bulk properties the phase switch method is used. In this method, a distributed Ordinary Differential Equation (ODE), with zero initial condition, is defined and solved at all time-steps and locations in the powder domain:

$$\frac{du}{dt} = T > T_m \tag{9}$$

In the phase switch method, variable u is equal to 0 for powder and 1 for bulk material representing different forms of the material. In this study, five commercially available AM alloys have been selected to simulate and study the effects of material properties on melt-pool development, temperature field evolution, and cooling rates. These alloys include IN718, IN625, stainless steel 316L, Ti-6Al-4V, and AlSi10Mg. The results of these studies are presented in later sections. Figure 3.5(a) and Figure 3.5(b) represent the powder and bulk thermal conductivity and density of the different material systems, respectively. Moreover, Figure 3.5(c) depicts the modified specific heat capacity of the different materials calculated through the Apparent Heat Capacity Method. It must be mentioned that in Figure 3.5(a), the thermal conductivity of the liquid phase in increased by factor C_m which is introduced in Section 3.1.6 and tabulated in Table 3.1. These thermo-physical properties are mainly extracted from Mills Handbook [86].
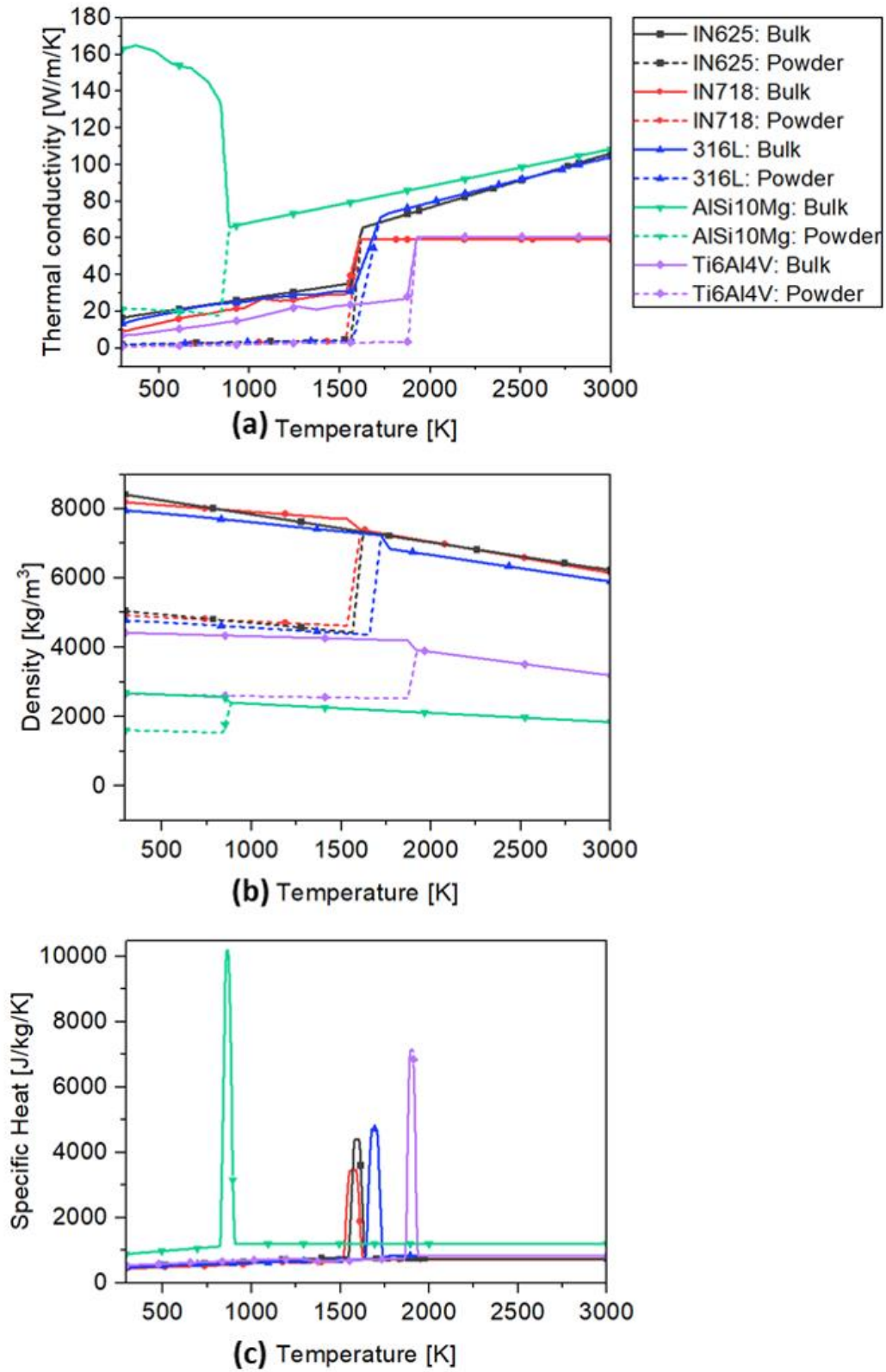
Figure 3.5: Powder and bulk thermo-physical properties of the five alloys of interest.

3.1.5 Evaporation

At high energy inputs, the temperature of the molten material exceeds the boiling

temperature of the alloy and causes evaporation. During evaporation, evaporated material is

removed by the flow of the shielding gas and the remaining material cools rapidly and solidifies

[23]. In the proposed CTM, however, mass loss due to evaporation is neglected for simplicity.

But it is worth mentioning that several studies have accounted for mass loss due to evaporation

by setting the density and specific heat capacity of the removed material to those of alloy gas

[23,87]. These methods assume that the removed material remains in gaseous state as

temperatures cool down.

As mentioned earlier, heat loss due to evaporation is implemented by a new physics-based

approach introduced by Karayagiz *et al.* [36]. In this approach, a heat sink is introduced on the

surface of the powder bed through following equations:

$$q_{evaporation} = -L_v \dot{m}_v$$

$$\dot{m}_v = P_{recoil} \sqrt{\frac{M}{2\pi RT}} \tag{10}$$

$$P_{recoil} = P_0 \, exp\left\{\frac{M \, L_v}{R}\left(\frac{1}{T_b} - \frac{1}{T}\right)\right\}$$

where L_v is latent heat of vaporization, $\dot{m}_v$ is the evaporative mass rate, P_{recoil} is the recoil

pressure, M is the molar mass of the material, R is gas constant, P_0 is atmospheric pressure, and

T_b is the boiling temperature of the alloy material.

The last two equations in Equation 10 are the Hertz-Knudson equation and the Clausius

Clapeyron equation, respectively. Some studies include a positive fraction in the equation for $\dot{m}_v$

as an adjustment factor to account for condensation on the surface [60]. However, there are many

discrepancies in the values reported in the literature. In this dissertation, it is assumed that no

condensation takes place and hence maximum heat flux happens. Accounting for evaporation has

a significant effect on heat loss and hence thermal field and melt-pool sizes. These effects are

described in detail in Section 6.1.

3.1.6 Marangoni Convection

Surface tension gradients on the surface of the melt-pool are due to spatial gradients of

temperature. These surface tension gradients generate Marangoni force which is the main driver

for fluid flow circulation (i.e., convection) inside the melt-pool. Marangoni or thermocapillary

convection is a critical phenomenon in fluid flow models of LPBF processes, specifically at high

energy inputs where the temperature gradients across the melt-pool are larger. As briefly

mentioned earlier in the chapter, surface tension gradients are also affected by chemical

concentration gradients. Therefore, for simplicity, the powder and the substrate are assumed to

be of the same material to avoid any mixing of different alloys and resulting surface tension

gradients. In order to estimate the strength of convective transport of heat in the melt-pool, a

non-dimensional number, called the Marangoni number (Ma) can be utilized:

$$Ma = -\frac{d\sigma}{dT}\frac{w\,\Delta T}{\mu\alpha} \tag{11}$$

where $\frac{d\sigma}{dT}$ is the rate of surface tension changing with respect to temperature, w is the

characteristic length of the molten pool (taken as the width of the melt-pool), ΔT is the

temperature difference between peak temperature inside the melt-pool and solidus temperature of

the alloy, μ is the dynamic viscosity, and α is the thermal diffusivity.

Higher values of Ma indicate that convection in the melt-pool is mainly driven by surface

tension gradients whereas small values indicate that there is no flow as diffusion dominates.

Marangoni convection has a critical effect on melt-pool geometry specifically. Traditionally, this

has been studied using CFD simulations that are computationally expensive and cumbersome. However, the effects of Marangoni convection can be approximated by increasing the thermal conductivity of the liquid phase by correction factor C_m. This value is either calculated experimentally or numerically and is reported in literature for many common alloys. This common approach has previously been utilized by several modelers, including Nikam *et al.* [37] and Ladani *et al.* [38], to numerically account for effects of Marangoni convection in the heat transfer model. The reported factors are extracted from references which are cited in Table 3.1. Section 6.2 covers the effects of accounting for Marangoni convection on the melt-pool sizes.

3.1.7 Process-induced Micro-voids

Implementation of process-induced micro-voids is one of the novelties of the CTM. Void formation can be realistically predicted with high-fidelity interface-tracking CFD simulations. However, the proposed modeling approach offers an efficient yet effective way of introducing micro-voids in the scanning domain. Accounting for micro-voids has a huge effect on thermal field (as shown in Section 6.3) as well as the thermo-mechanical field during the multi-layer deposition process. As mentioned in Section 2.2.2, there are many factors that lead to formation of undesired voids during the printing process which makes predicting and avoiding voids a difficult task.

In the proposed CTM, process-induced micro-voids are randomly implemented in the model through defining thermo-physical properties with random spatial distributions generated using Equation 12 [88]. The idea behind this implementation is to generate a random spatial distribution of values and use them in defining material properties. Initially, powder properties are assigned and as the laser scans and melt-pool solidifies, properties ranging from air to bulk material are randomly assigned to replicate the inhomogeneous nature of printed parts in the

44

presence of voids. Function $f(x, y, z)$, as presented below, produces a spatially random number through a triple sum expression for a 3D volume:

$$f(x, y, z) = \sum_{k=-K}^{K} \sum_{l=-L}^{L} \sum_{m=-M}^{M} a(k, l, m) \cos\big(2\pi(kx + ly + mz) + \emptyset(k, l, m)\big)$$

$$a(k, l, m) = g(k, l, m)\, h(k, l, m) = \frac{g(k, l, m)}{(k^2 + l^2 + m^2)^{\beta/2}}$$

(12)

where $g(k, l, m)$ is the amplitude coefficient with a Gaussian distribution, $h(k, l, m)$ is the frequency-dependent amplitude, β is the spectral exponent, and $\emptyset(k, l, m)$ is the phase angle with uniform random distribution. K, L, and M are integers corresponding to maximum frequency in each direction. Therefore, the thermo-physical properties are assigned as follows:

$$u = \begin{cases} 0 & \begin{aligned} &\rho_{powder}(T), k_{powder}(T) \end{aligned} \\ 1 & \begin{aligned} &\rho_{mean} + Af(x, y, z) \\ &k_{mean} + Bf(x, y, z) \end{aligned} \end{cases}$$

(13)

where constants A and B are chosen such that the minimum value of the calculated thermo-physical property, namely density and thermal conductivity, of the powder bed corresponds to air and the maximum value corresponds to bulk properties of the resulting alloy. $u = 0$ corresponds to powder properties and $u = 1$ corresponds to properties assigned after solidification takes place. To better illustrate this approach, Figure 3.5 presents the introduction of pores in the scanning domain during printing. In this figure, the spotty blue areas in the powder domain represent voids with properties resembling that of air. The material used here for demonstration purposes is stainless steel 316L.
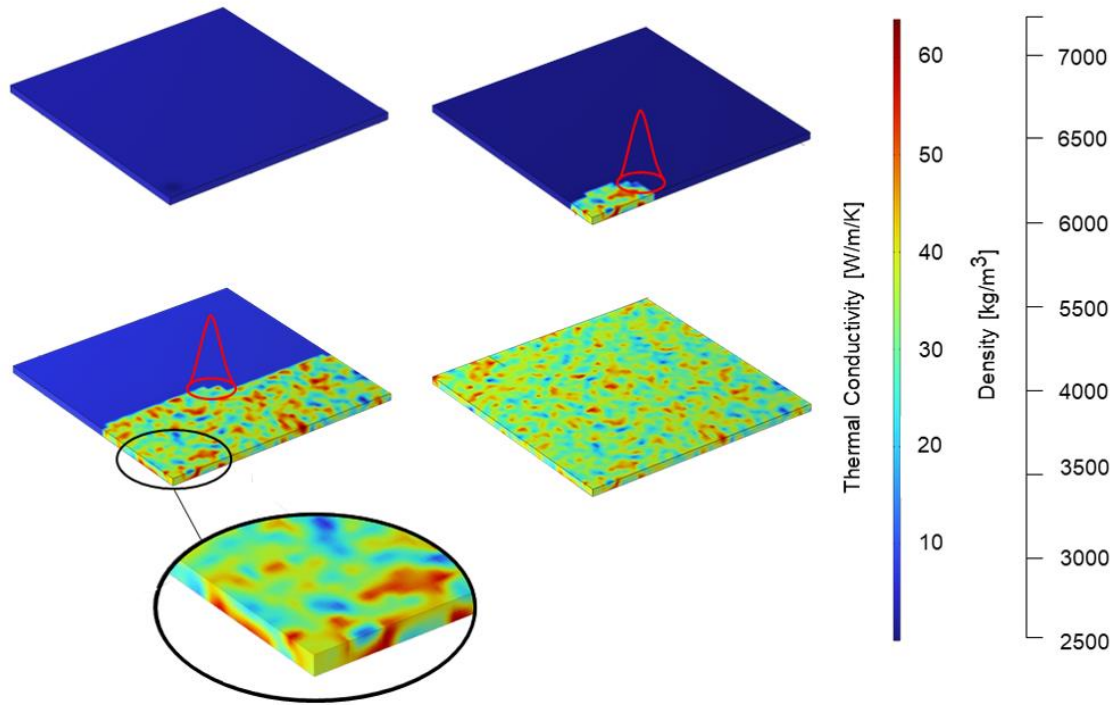
Figure 3.6: Graphical representation of the implementation of micro-voids in the scanning domain and spatially random thermo-physical properties ranging from air to bulk properties

Pore morphologies, as depicted in Figure 3.7, are dependent on the mechanism leading to the formation of pores. Plessis [89] developed 3D images from X-ray tomography of a series of Ti-6Al-4V samples. According to his findings, lack-of-fusion voids are irregular in shape and size with occasional entrapment of un-melted powder particles. These voids are elongated (length $> 100 \ \mu m$) and narrow in shape and generally oriented perpendicular to the building direction. On the other hand, keyhole-induced pores are rounded (diameter $> 50 \ \mu m$) while gas pores are near-spherical and much smaller in size. In addition to characterizing pores in terms of their shapes, some studies have also provided statistical data on their morphologies based on experimental measurements. For instance, Kasperovich *et al.* [90] evaluated pores statistically

using descriptors such as circularity, sphericity, aspect ratio, and convexity. Circularity (C) and

sphericity (ψ) are defined through the following two equations:

$$C = \frac{4\pi \cdot A_s}{L^2}$$

$$\psi = \frac{6\pi^{0.5} \cdot V}{A^{1.5}}$$

(14)

where A_s is pore surface area, L is pore perimiter, and V is pore volume. Sphericity is equal to

one for a perfect sphere and approaches zero for more irregular and elongated pores. To increase

the practicality and effectiveness of the proposed approach in implementation of process-induced

micro-voids, statistical data from actual experimental measurements can be used to replicate a

more realistic representation of generated micro-voids during printing. However, in this

dissertation, the objective is to prove that the proposed methodology has potential. Therefore,

incorporation of experimental measurements can certainly be subject of future studies.
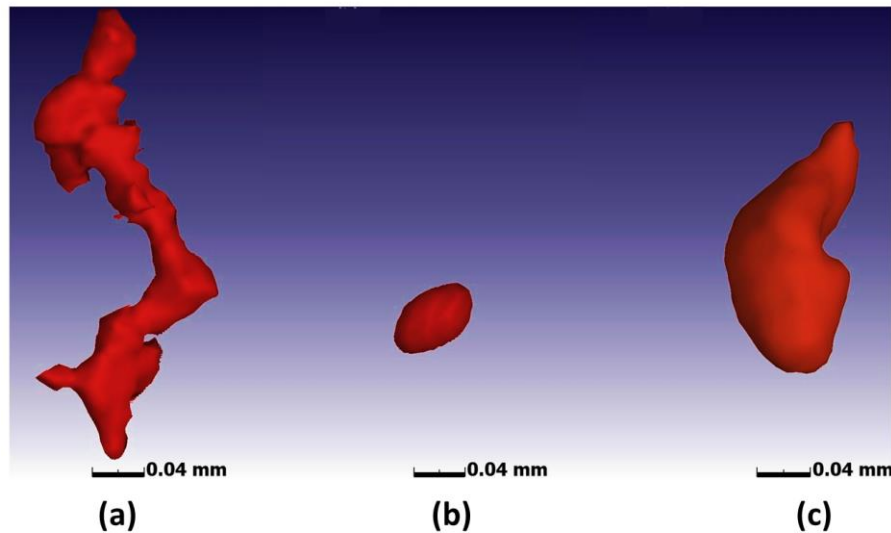

Figure 3.7: Pore morphologies of LPBF parts as characterized by Plessis [89] are (a) lack-of-fusion

pores, (b) gas pores, (c) keyhole-induced pores.

3.1.8 CTM-specific Parameters for Alloys of Interest

The parameters discussed in Sections 3.1.1-3.1.7, are extracted from literature for different

materials and tabulated in Table 3.1. These parameters are used in running CTM simulations and

generating the results discussed in Chapter 4.

*Table 3.1: CTM-specific parameters for the five alloys of interest. (Values with * are not readily*

available in literature and hence, have been estimated based on the values for similar materials.)

Parameters	Material System					Ref.
	IN625	IN718	316L SS	Ti-6Al-4V	AlSi10Mg	
A_m	0.27	0.30*	0.34	0.39	0.30*	[91]
$L_f\ (\frac{kJ}{kg})$	227	210	260	286	293	[86]
$L_v\ (\frac{kJ}{kg})$	6000	5800	6100	9830	12000	[86]
$T_s(K)$	1563	1533	1658	1878	798	[86]
$T_m(K)$	1623	1609	1723	1923	898	[86]
$T_b(K)$	3100	3190	3086	3315	2700	[86]
$M(\frac{g}{mol})$	59.57	57.94	55.85	446.06	27.00	[86]
C_m	2	2	2.5*	1.76	1*	[37,92,93]

3.1.9 Successive Addition of layers

Another important feature of the CTM is modeling successive deposition of powder layers

which is important in the simulation of the multi-layer deposition process. The energy introduced

by subsequent passing of the laser on new layers has a profound effect on the temperature field,

cooling rates, and melt-pool dimensions. A common approach to simulate addition of layers with

time is the method of "element birth and death" [94,95]. In this technique, the entire 3D

geometry is constructed first where all the elements are initially deactivated. In other words, the

elements are visually present, yet they do not add to the overall stiffness matrix before they are

48

activated. As the laser scans, the elements within the layer are activated and appropriate thermo-physical properties are assigned to them.

In this dissertation, to simulate addition of new layers, temperature field obtained from the FE analysis of the nth layer is mapped to the corresponding locations as initial condition for simulation of the n+1th layer. The new layer, which is in the powder state before the laser scans, is assumed to be at room temperature. The deposited layer is added to the existing geometry and the entire geometry is re-meshed after each deposition. The deposition of subsequent layers is automated using nested loops in the MATLAB scripts.

3.2   Thermo-mechanical Modeling based on CTM

As part of the SMM approach, the transient CTM can be coupled with a mechanical model to study the thermo-mechanical response of alloys. The 3D simulation can be used to predict the state of stress and deformations at any stage of the manufacturing process. The *Heat Transfer* and *Structural Mechanics Modules* in COMSOL Multiphysics were utilized to develop a coupled FE thermo-mechanical model. Among the governing equations are the equilibrium equation and the stress-stain constitutive relation, respectively, as presented below:

$$\sigma_{ij,j} = 0$$

$$\sigma_{ij} = C_{ijkl}\,\varepsilon_{kl}{}^{el}$$

(15)

where σ_{ij} is the stress tensor, C_{ijkl} is the modulus tensor, and $\varepsilon_{kl}{}^{el}$ is the elastic strain. Plastic strain is neglected in the present thermo-mechanical model due to lack of reliable information about thermo-elastic-plastic parameters. Hence, the material is assumed to be linearly elastic and the total strain is defined as the sum of elastic and thermal strains:

$$\varepsilon_{ij}{}^{total} = \varepsilon_{ij}{}^{el} + \varepsilon_{ij}{}^{th}$$

(16)

$$\varepsilon_{ij}{}^{el} = \frac{1}{2}\left(u_{j,i} + u_{i,j}\right)$$

$$\varepsilon_{ij}{}^{th} = \alpha_e(T - T_0)$$

where α_e is the temperature-dependent coefficient of thermal expansion and u is the displacement field. For simplification, material is assumed to be isotropic as well as linearly elastic with C_{ijkl} defined as following:

$$C_{ijkl} = \lambda\, \delta_{ij}\delta_{kl} + \mu\left(\delta_{ik}\delta_{jl} + \delta_{il}\delta_{jk}\right)$$

$$\lambda = \frac{\nu E}{(1+\nu)(1-2\nu)} \tag{17}$$

$$\mu = \frac{E}{2(1+\nu)}$$

where ν is Poisson's ratio, E is Young's modulus, and δ is Dirac delta function. The defined C_{ijkl} in Equation 17 is the most general isotropic 4th-order modulus tensor where λ and μ are Lame constants that are in terms of material's properties [96]. Young's modulus is a measure of the stiffness of the material or its resistance to deformation when subjected to stresses, and ν is the Poisson's ratio which measures the lateral contraction produced by the applied stress.

To minimize errors in stress predictions, temperature-dependent Young's modulus and coefficient of thermal expansion, for bulk and powder material, are used and extracted from the following references [86,97,98]. However, to get more realistic results, it is essential to account for plasticity rather than considering a perfectly-elastic model. Strains induced because of the solid-state phase transition can also be considered to increase the accuracy of the thermo-mechanical model. Such strains are, however, neglected in most macroscopic thermo-mechanical models of multi-layer LPBF processes [42]. When considering these two effects, the equation for total strain would be:

$$\varepsilon_{ij}{}^{total} = \varepsilon_{ij}{}^{el} + \varepsilon_{ij}{}^{th} + \varepsilon_{ij}{}^{p} + \varepsilon_{ij}{}^{v} \tag{18}$$

where $\varepsilon_{ij}{}^{p}$ and $\varepsilon_{ij}{}^{v}$ are plastic and strain induced by solid state phase transformation,

respectively. Several of the existing thermo-mechanical models, consider plastic strain and the

cyclic work hardening effect using a plasticity model with the von Mises yield criterion [42,99].

Although the plastically deformed regions are small in size in LPBF parts, they increase the

computational costs significantly because of non-linear material behavior [60]. The effects of

accounting for Marangoni convection and evaporation on the linearly-elastic thermo-mechanical

response of the part are described in Section 6.4.

3.3 Data-driven and Physics-informed ROM

The presented physics-based model is accurate and efficient enough to be used as a rapid

computational tool for extracting datasets and developing a data-driven or a physics-informed

ROM. The main benefit of the ROM over the physical model is its efficiency and speed in

providing near-real-time or sub-second predications. Therefore, in this dissertation, a CNN

architecture has been proposed to develop a ROM or specifically, train a CNN using datasets

extracted from the physics-based model. Figure 3.8 represents the workflow as well as a

schematic for the proposed CNN architecture. In this workflow, during the multi-layer deposition

process, the temperature field at every time-step is discretized into a certain number of cuboids

of height of the powder layer thickness and a temperature is assigned to each cuboid using shape

functions. These values are stored in the form of 3D arrays of temperature data and labelled as

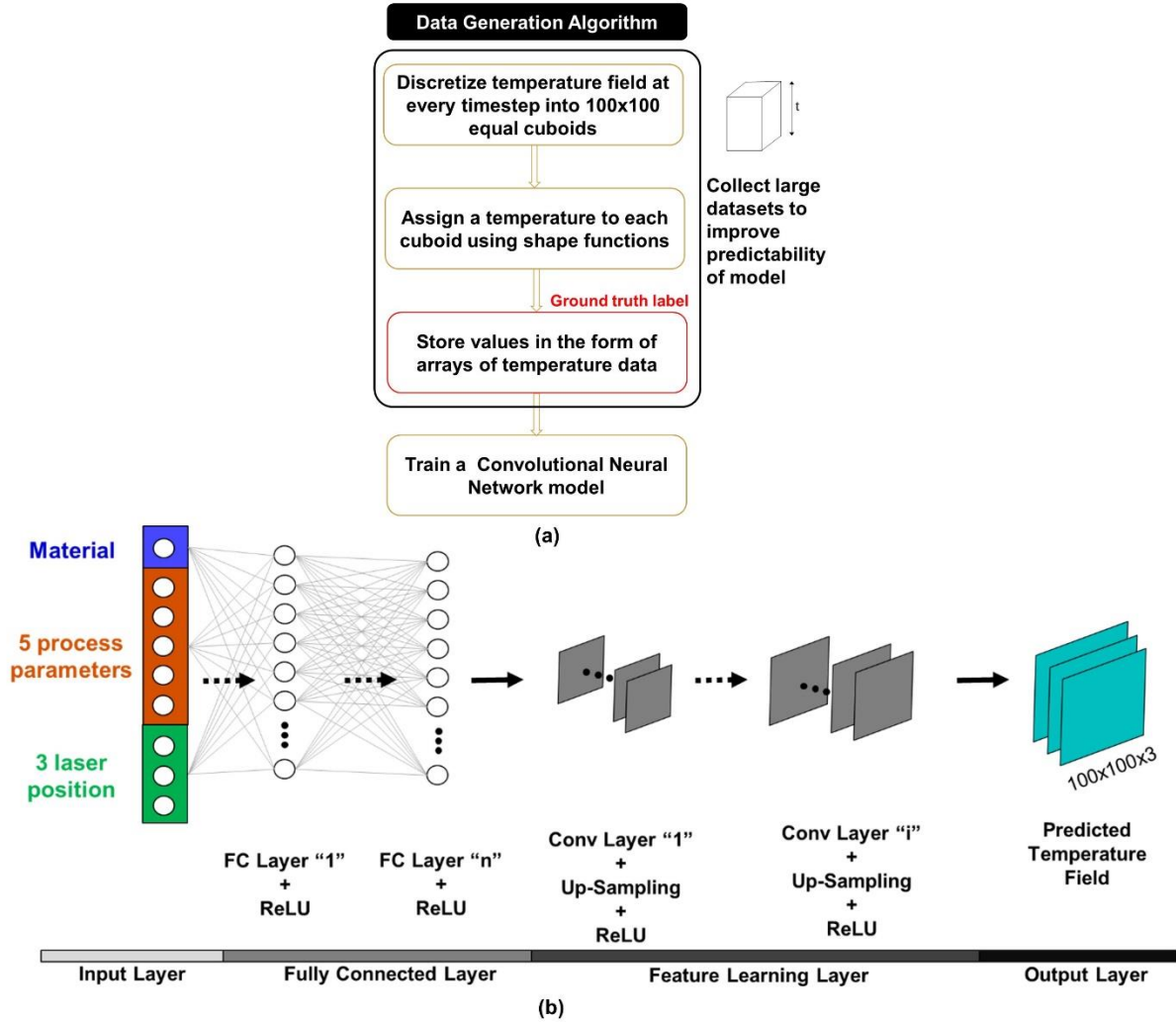the ground truth in the model.

Figure 3.8: (a) The proposed workflow, and (b) a schematic of the proposed CNN architecture for sub-second prediction of the temperature field for a 3-layer LPBF simulation

For instance, for a 3-layer deposition process and assuming the temperature field is discretized into 100×100 cuboids, an array of size $100 \times 100 \times 3$ would be extracted at every time-step. The array needs to be flattened into a single column in the data pre-processing step. Inputs to the network could be material specifications, five process parameters (i.e. laser power, laser velocity, hatch spacing, powder layer thickness, and laser beam radius), and 3 laser position parameters (i.e. x, y, and z coordinates of the laser). These 9 laser and powder properties in

addition to manufacturing process parameters would get inputted into the network and pass through a few fully connected layers. The last fully connected layer would then be reshaped into multiple small 2D arrays of numbers. Using up-sampling and convolutional operation, these relatively small (2D) arrays would then be decoded into larger 2D images. At every stage, the number of 2D arrays gets reduced until the output layer with 3 layers of 100×100 2D array of numbers. These 30,000 output numbers would then be compared to the ground truth label to calculate the loss as well as optimize the weights and biases using the backpropagation algorithm.

In order to determine the optimal hyper-parameter settings, it would be useful to take a random subset of data and look at several combinations of hyper-parameters which include number of filters in convolutional layers, number of neurons per fully connected layer, and the learning rate. The learning rate is used to decide by how much the weights are updated or how quickly the loss function is minimized after each iteration. In this dissertation, the objective is to propose the CNN architecture that can be utilized for developing a ROM using the presented physics-based model. Another promising use case for the proposed physical model is training a physics-informed CNN model that incorporates physical laws and physics-informed loss functions based on the governing PDEs. However, due to limited computational resources, implementation of such frameworks is beyond the scope of this dissertation and would be subject of future studies.

Chapter 4.   Results Obtained from the CTM

     This chapter aims to present, discuss, and compare the results obtained from the CTM for the five-layer deposition simulations of the five alloys of interest: IN718, IN625, stainless steel 316L, Ti-6Al-4V, and AlSi10Mg. Section 4.1 focuses on the thermal history signatures at a specific location in the scanning domain and studies the re-melting of previous layers. Section 4.2 discusses the surface cooling rates at the corresponding locations and analyzes their correlation with the stress development. Lastly, Section 4.3 compares the melt-pool dimensions across the materials as five layers are deposited and discusses the factors that affect these differences. Table 4.1 presents the process parameters used in running these simulations including powder layer thickness (t_p), laser power (P), laser velocity (V_s), and hatch spacing (h). The first column of the table indicates the process parameters under consideration and the last column represents the average values for the aggregate of all the materials considered across each row. Table 4.2 also presents the remaining process parameters including initial temperature (T_0), laser radius (ω), and initial powder density (ϕ_0) as well as atmospheric pressure (P_0) and gas constant (R).

Table 4.1: Representative process parameters used in running simulations

Parameters	Material System					Representative Values
	IN625	IN718	316L SS	Ti-6Al-4V	AlSi10Mg	
$t_p (\mu m)$	20	25	40	20	50	30
$P\ (W)$	195	100	280	180	175	185
$V_s\ (\frac{mm}{s})$	800	600	500	900	1025	765
$h (\mu m)$	100	35	$40 - 70$	80	100	75
Ref.	[11]	[100]	[101]	[102]	[103]	-

Table 4.2: The remaining process parameters and constants as defined in simulations

Parameters	Values
$T_0(K)$	293
$\omega(\mu m)$	50
ϕ_0	0.4
$P_0(atm)$	1
$R\left(\frac{kJ}{kmol.K}\right)$	8.314

4.1 <u>Thermal Signatures</u>

In the melting process, thermal histories of the powder bed are rapidly changing with time, with the maximum temperature happening on the powder layer surface at the center of the laser beam and decreasing with distance from the center of the beam which assumes to follow a Gaussian distribution. Predicting thermal histories is critical since they majorly govern microstructural evolution and grain structure. Figure 4.1 shows the computed temperature fields for IN718 as five layers are deposited. The thermal history of point A, as indicated in Figure 4.2, is tracked during the five-layer deposition process for the five material systems considered here. Point A is a point from which the laser passes; hence it experiences the highest temperatures during the scanning of the first layer. As layers are deposited and the heat source moves away, the peak temperatures drop down at point A and everywhere else in the lower layers.
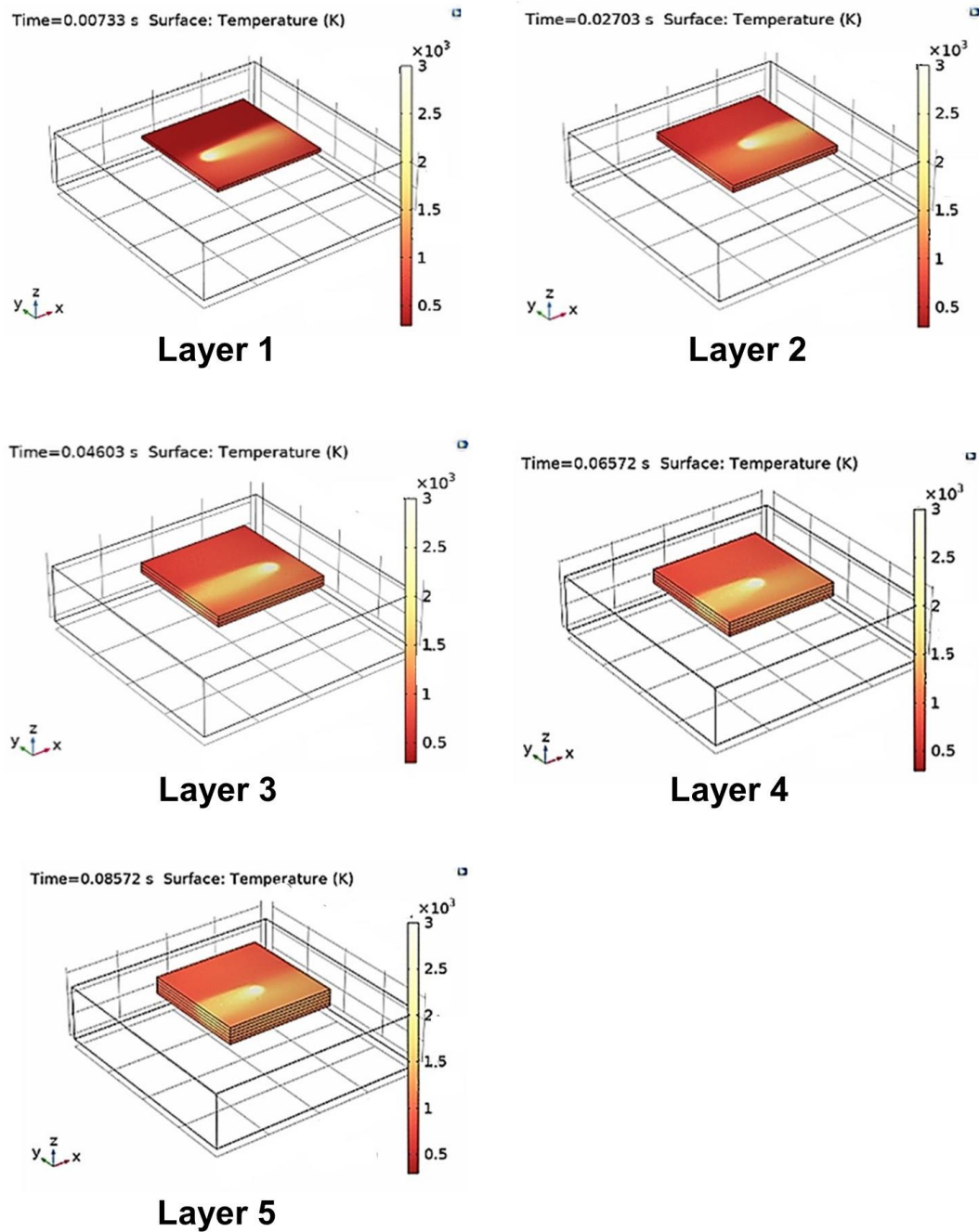
Figure 4.1: Temperature distribution during the five-layer deposition of IN718 using CTM

By comparing the peak temperatures after the deposition of new layers with the melting temperature of the material, one can determine how much re-melting of the previous layers happens. In Figure 4.2, the blue line indicates the melting temperature for each alloy. It can be

seen that with this specific set of process parameters, AlSi10Mg alloy experiences re-melting of all previously deposited layers as all five peak temperatures exceed the melting temperature of the alloy. This is due to the alloy's higher thermal conductivity and lower melting temperature compared to the rest of the alloys under study. On the other hand, Ti-6Al-4V experiences the lowest peak temperature compared to the rest of the alloys. An important note to make is that due to the consideration of evaporative heat loss in this model, the peak temperatures are realistic and roughly around the boiling temperature of each alloy.
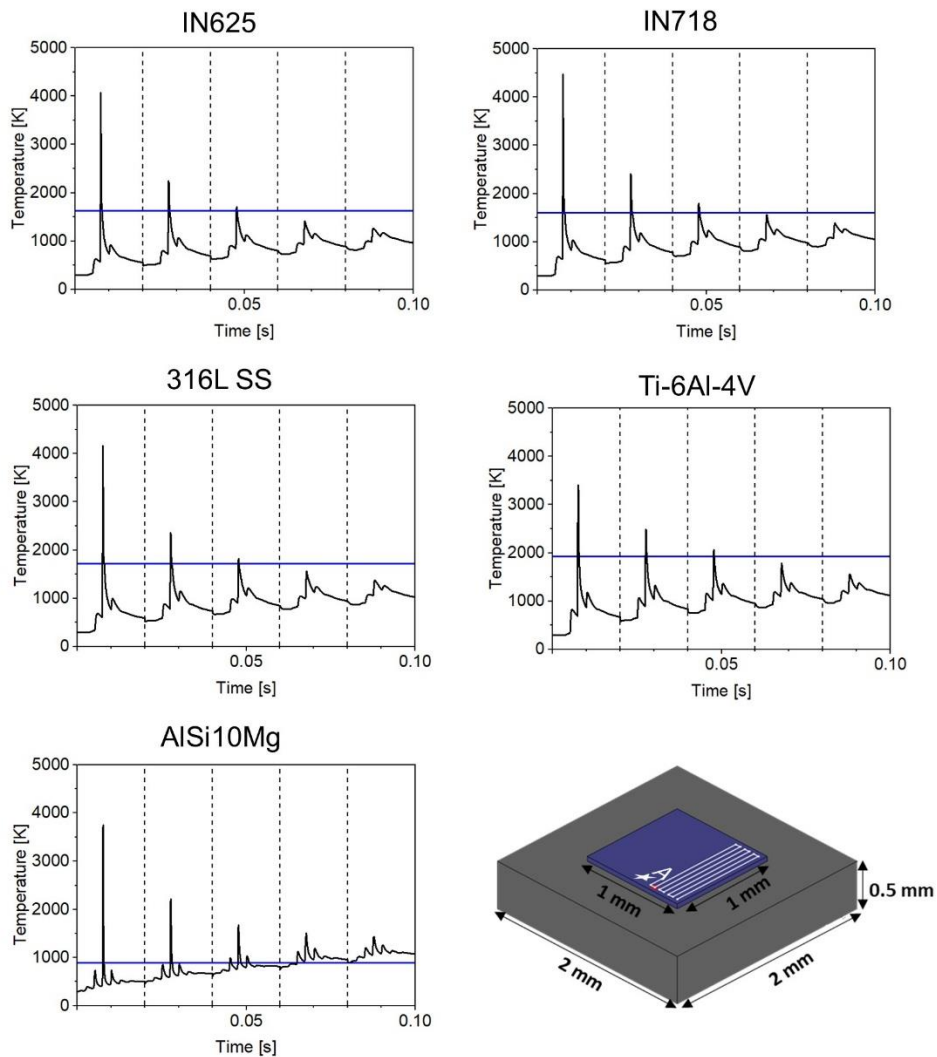
Figure 4.2: Thermal histories of the five alloys of interest in point A

4.2 <u>Surface Cooling Rates</u>

Cooling rate is defined as the rate at which the temperature decreases with time and it is identified as one of the most important factors in AM processes, in general. In any metal AM, depending on the process parameters and the energy input, the cooling rates are generally high and range from 10^4 to 10^6 K/s. Accurate prediction of cooling rates and thermal gradients are essential as they directly control the microstructure development and grain structure during the multi-layer deposition process. Cooling rates are also directly correlated with residual stress development and hence are essential to be accurately predicted. In fact, several existing studies have focused on optimizing process parameters and scan strategies to identify local defect-prone locations and control cooling rates for local microstructure development [104].

Figure 4.3 illustrates the surface cooling rates for the five materials of interest as predicted by the CTM. An important observation from Figure 4.3 is that Ti-6Al-4V experiences the highest cooling rates during the scanning of the first layer and hence is more prone to higher residual stresses and microstructural defects. Also, one can see that the peak values occur immediately after the laser passes and the cooling rate slows as solidification takes place and heat stores as latent heat of fusion is dissipated. However, the cooling rates certainly vary depending on the process parameters used as well as the selected location in the scan path.
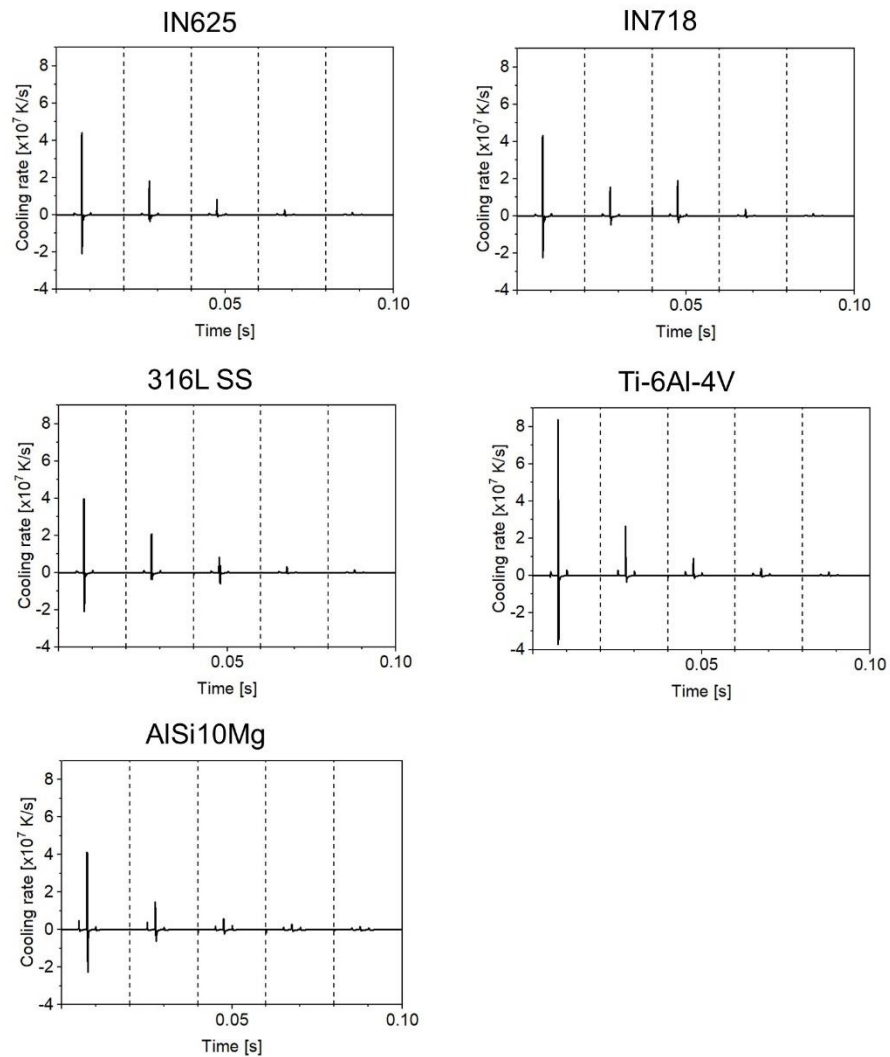
Figure 4.3: Corresponding surface cooling rates of the five materials under study during the five-layer deposition process

4.3 Melt-pool Development

With the thermal model developed, it is also possible to obtain the melt-pool size and geometry using isothermal contours (as depicted in Figure 4.4), using the melting temperature of the alloy as the minimum temperature. Melt-pool dimensions are affected by the material properties as well as process parameters and are directly correlated with part quality,

59

microstructure evolution, and additional implications. Hence, an accurate prediction of melt-pool

evolution during LPBF process is critical. On one hand, small melt-pool sizes make the AM

process inefficient by increasing the processing time as well as reducing density and hindering

part quality. On the other hand, large melt-pool sizes can cause excessive vaporization and hence

increased porosity in the printed structure. Therefore, many existing studies have focused on

optimizing process parameters, either numerically or experimentally, in an effort to achieve

stable melt-pool sizes [11].
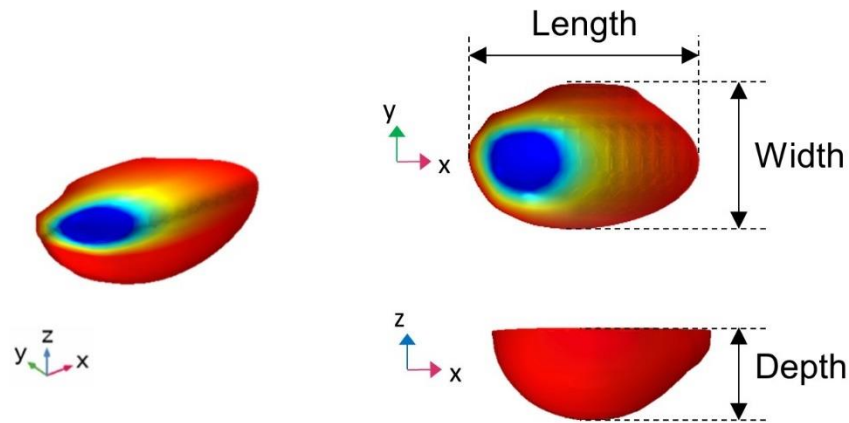
Figure 4.4: A graphical representation of melt-pool length, width, and depth

Figure 4.5 and Figure 4.6 compare the melt-pool geometries during the five-layer

deposition process for the five alloys of interest. An important observation from these two

figures is that the size of the melt-pool increases as new layers are added. This is mainly due to

heat transfer from the lower layers. Also, it can be seen that alloy composition hugely affects the

thermal field and hence leads to different melt-pool sizes during the five-layer deposition

process. Due to its unique thermal properties, the size of AlSi10Mg melt-pool is much larger

than the rest of the materials as can be seen in Figure 4.5. This unstable behavior is also

evidently observed in Figure 4.2. Therefore, it can be concluded that the representative process

parameters used in these simulations are more aggressive and intense for AliSi10Mg compared

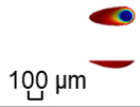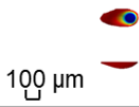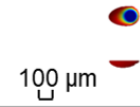to the optimized process parameters listed for the alloy in Table 4.1.
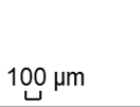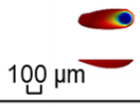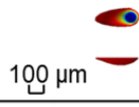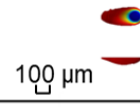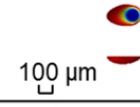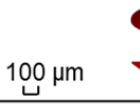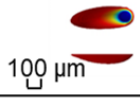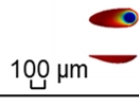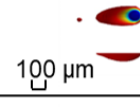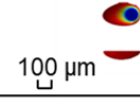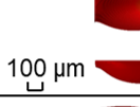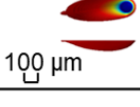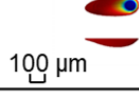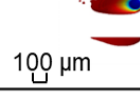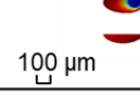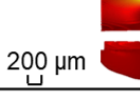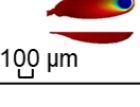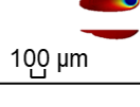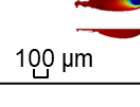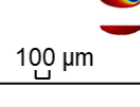
	IN718	IN625	316L	Ti-6Al-4V	AlSi10Mg
Layer 1	100 μm	100 μm	100 μm	100 μm	100 μm
Layer 2	100 μm	100 μm	100 μm	100 μm	100 μm
Layer 3	100 μm	100 μm	100 μm	100 μm	100 μm
Layer 4	100 μm	100 μm	100 μm	100 μm	200 μm
Layer 5	100 μm	100 μm	100 μm	100 μm	Out of Range

Figure 4.5: A graphical comparison between melt-pool dimensions for the five materials of interest as

five layers are deposited
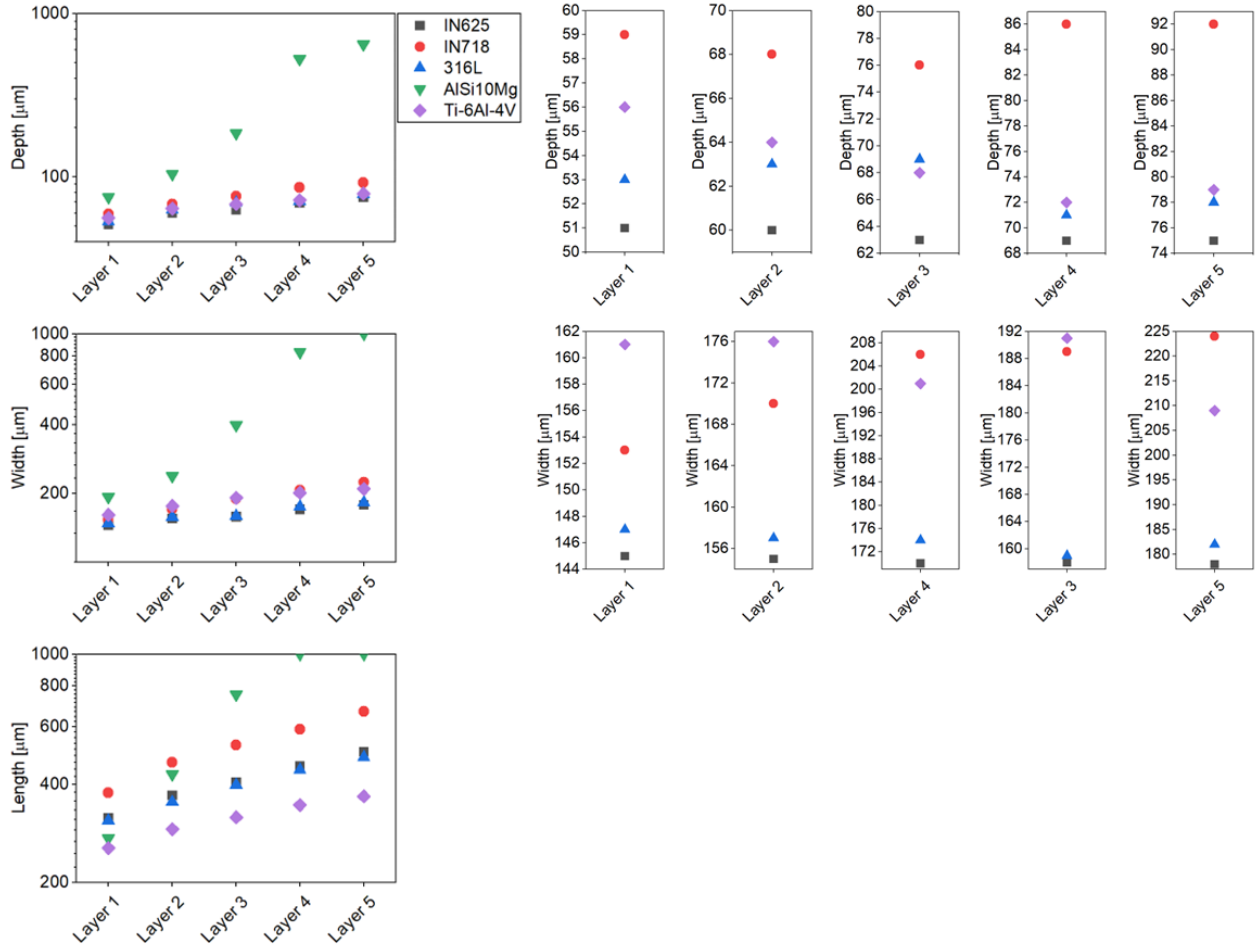
Figure 4.6: A comparison between depth, width, and length of the melt-pools across different alloys

Chapter 5.   Experimental Verification of the CTM

To prove the fidelity of the proposed thermal model, the CTM is verified using the measurements provided by Karayagiz *et al.* [36]. The mentioned reference presents experimental data on thermal history and melt-pool widths during LPBF of Ti-6Al-4V using the zigzag scanning pattern. The process parameters used in the experiments and the corresponding simulation using CTM are listed in Table 5.1. The simulation domain is presented in Figure 5.1 with a thin layer of powder over a bulky substrate of the same material. In order to ensure consistency with the referenced literature, the same 8-noded hex mesh of size 25 µm for the powder bed and much coarser tetrahedral mesh for the substrate were used.

The comparisons between experimental and numerical thermal histories at a point in the scanning domain are presented in Figure 5.1. It is clear from this figure that there is good agreement between the numerical values from CTM and experimental measurements. According to [36], the discrepancies can be mainly due to noise in temperature measurements made using a thermal imaging sensor with high-speed thermography. Considering the constant spattering and instabilities of the printing process, accurate in-situ temperature measurements are generally very difficult to obtain. In LPBF processes, many of the phenomena occur at a very short time span of just a few microseconds and hence are not easy to measure using typical measuring instruments.

Moreover, the width of the melt-pool measured from experiments is reported to be 170 ± 13 µm and the proposed CTM predicts 172 µm. Therefore, the prediction error of the CTM is within an acceptable range which proves the accuracy of the proposed modeling approach in predicting thermal history and melt-pool dimensions during multi-layer LPBF.

Table 5.1: Process parameters used in experiment and corresponding CTM

Parameters	Values
$t_p(\mu m)$	30
$\omega(\mu m)$	35
P	50
$V_s(\dfrac{mm}{s})$	80
$h\ (\mu m)$	70
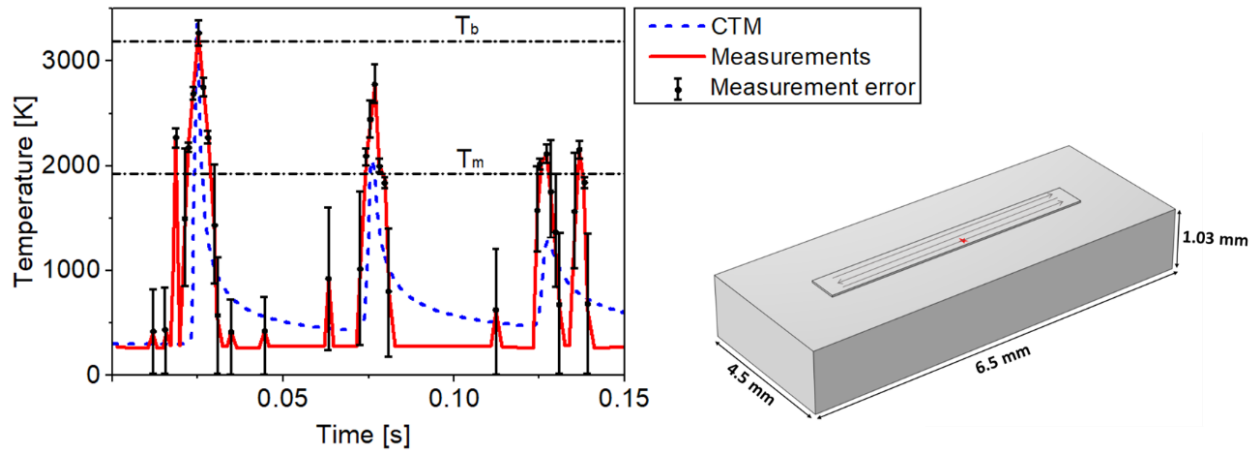
Figure 5.1: Comparison between experimental and numerical thermal histories at the location identified by a red star in the scanning domain

Chapter 6.   Evaluation of Effects of Fluid Flow on Thermal and Thermo-mechanical Response

This chapter aims to investigate the importance of accounting for fluid flow effects on the thermal and thermo-mechanical response of alloys. Sections 6.1 and 6.2 discuss the effects of Marangoni convection and evaporation on the thermal history signatures and melt-pool development through the deposition process, respectively. In other words, thermal histories and melt-pool dimensions are used as metrics for comparison of the results in the presence and absence of fluid flow phenomena. Section 6.3 aims to discuss the importance of accounting for micro-voids on the temperature field and hence the consequent thermo-mechanical response. Lastly, Section 6.4 discusses the effect of Marangoni convection and evaporation on the thermo-mechanical response of alloys during single layer LPBF.

6.1   Effect of Evaporation

As mentioned earlier, material evaporation at high energy densities can lead to defect formation during the printing process. Therefore, accounting for evaporation is crucial when modeling LPBF processes. Figure 6.1 represents the direct effect of evaporation on peak temperatures as well as melt-pool dimensions. Both simulations presented in Figure 6.1 were run using the representative set of process parameters tabulated in Table 4.1 during the five-layer deposition process for IN718. An important observation to make from Figure 6.1 is that the peak temperature in the presence of evaporation is much closer to the boiling temperature of IN718 (i.e. 3190K) as opposed to the unphysically elevated temperatures of conduction-only thermal models. In other words, when neglecting evaporation, the temperature of the melt-pool is not bounded by the evaporation temperature and hence this leads to excessive overheating of the melt-pool. Although accounting for heat loss due to evaporation has a significant effect on peak

temperatures, determining how much of this effect is a result of other features as opposed to evaporation solely, can be investigated through a quantitative and systematic sensitivity analysis in future studies.

In addition to overestimated peak temperatures, the size of the melt-pool is also unphysically and unrealistically large in the absence of evaporation as depicted in Figure 6.1. As it can be seen in this figure, neglecting heat loss due to evaporation results in melt-pools that reach the edge of the powder domain for layers 3, 4, and 5 hence it seems they are cut off on the edges. This comparison clearly demonstrates that considering evaporation in the CTM is of utmost importance and crucial in achieving results that align better with experimental measurements and hence lead to more accurate predictions when coupled with a mechanical model to investigate stresses and distortions.
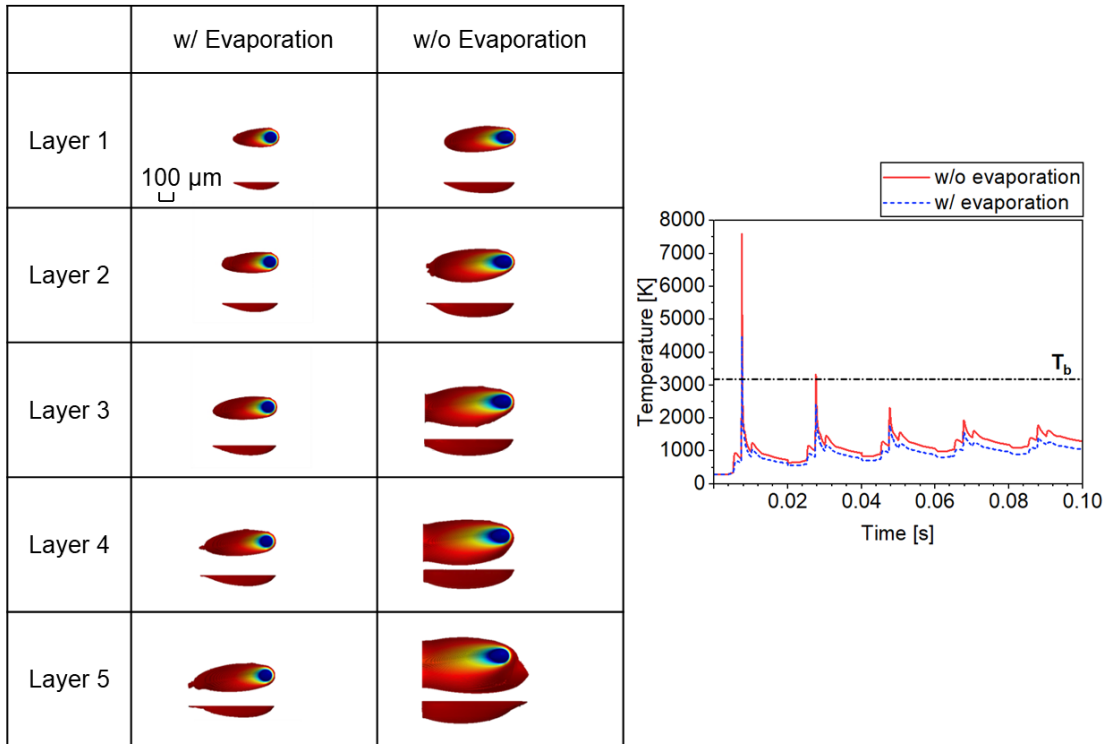
Figure 6.1: Comparison of melt-pool sizes and thermal histories in the presence and absence of heat loss due to evaporation

6.2   Effect of Marangoni Convection

Another fluid flow phenomenon that hugely affects the melt-pool size is the flow induced by Marangoni convection. This has been demonstrated through comparing the melt-pool sizes in the absence and presence of Marangoni convection effects in the CTM. As discussed in Section 3.1.6, to account for Marangoni convection in the CTM the thermal conductivity of the liquid phase is increased by correction factor C_m. Therefore, in the absence of this effect C_m is taken to be 1 and in the presence of this effect C_m is taken to be 2 (for IN718, see Table 3.1). The same set of representative process parameters provided in Table 4.1 are used to run both sets of simulations for five-layer deposition of IN718.

The melt-pool sizes are depicted in Figure 6.2. Based on the results, neglecting the Marangoni driven flow results in melt-pools that are unnaturally narrow and shallow whereas accounting for the effects leads to more realistic melt-pool sizes. According to Yuan and Gu [105], in the presence of Marangoni convection, the melt-pool would be wider, whereas neglecting Marangoni effects would lead to a narrower melt-pool shape. This is clearly observed in Figure 6.2 where significant discrepancies in width exist in the absence and presence of Marangoni convection.

The direction and strength of Marangoni convective flow is directly correlated with the surface tension gradients that are caused by temperature differences. Therefore, at higher energy inputs where larger temperature gradients exist, accounting for Marangoni convection is of utmost importance and critical in achieving accurate predictions of melt-pool sizes. Although Marangoni flow has a significant effect on melt-pool sizes, it was found that accounting for Marangoni convection has minimal effect on the peak temperatures during the deposition

process. Therefore, the thermal history signatures in the absence and presence of Marangoni effects are closely similar.
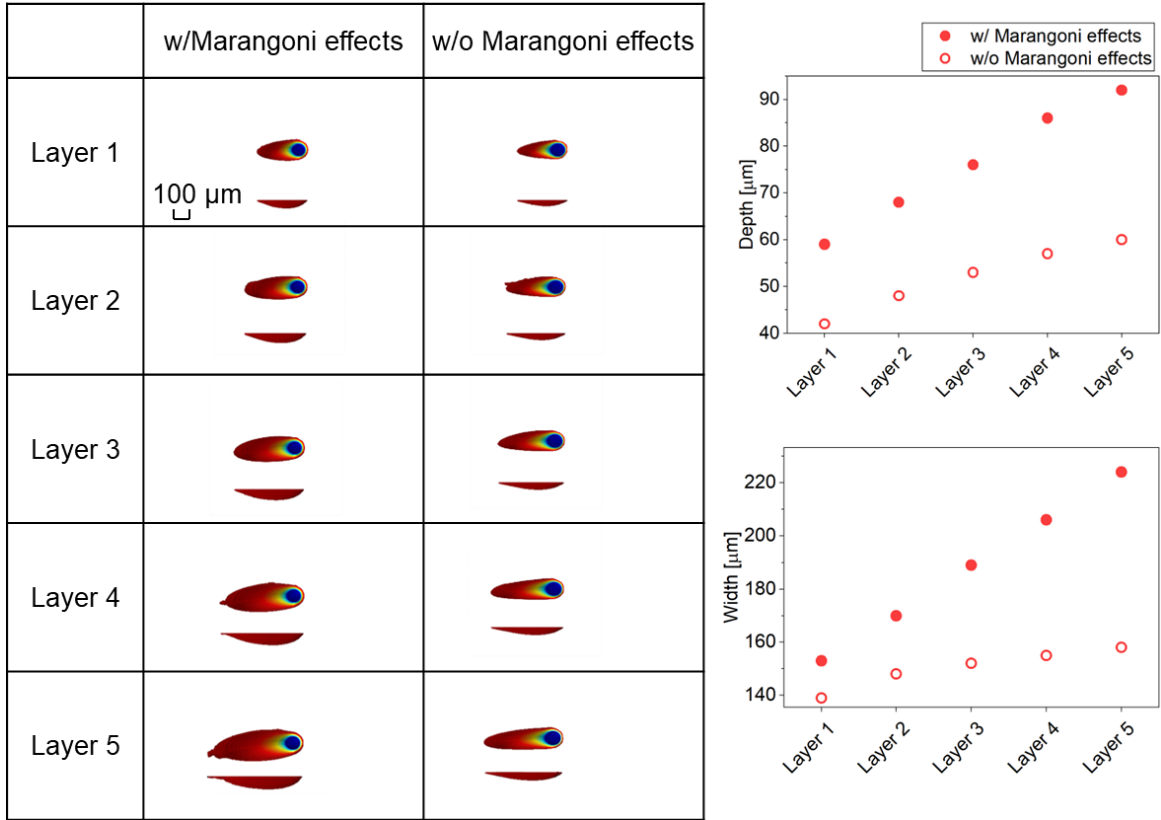
Figure 6.2: Comparison of melt-pool sizes in the presence and absence of Marangoni effects

6.3   Effect of Micro-voids on Temperature Field

The new approach developed in this dissertation, accounts for process-induced micro-voids using spatially random numbers in defining material properties. This is thoroughly described in Section 3.1.7. However, in order to more closely look at the effect of voids on the temperature field (before considering a collection of random pores in the scanning domain), the thermal histories were compared in the presence of a single void. Figure 6.3 represents the thermal histories in the presence of a spherical void positioned at a predefined location in the scanning

domain. This result is simulated using the same set of process parameters as provided in Table 4.1 and a scan length of 765 μm.

For demonstration purposes, the spherical void (with radius of 10 μm) is used as a simplified version of a random geometry of an actual void from experiments. Initially, the void has powder properties as if it does not exist in the domain. As the laser starts scanning and temperatures rise above the melting temperature of the alloy, air properties will be assigned to the void element to replicate presence of a micro-void in the powder domain.
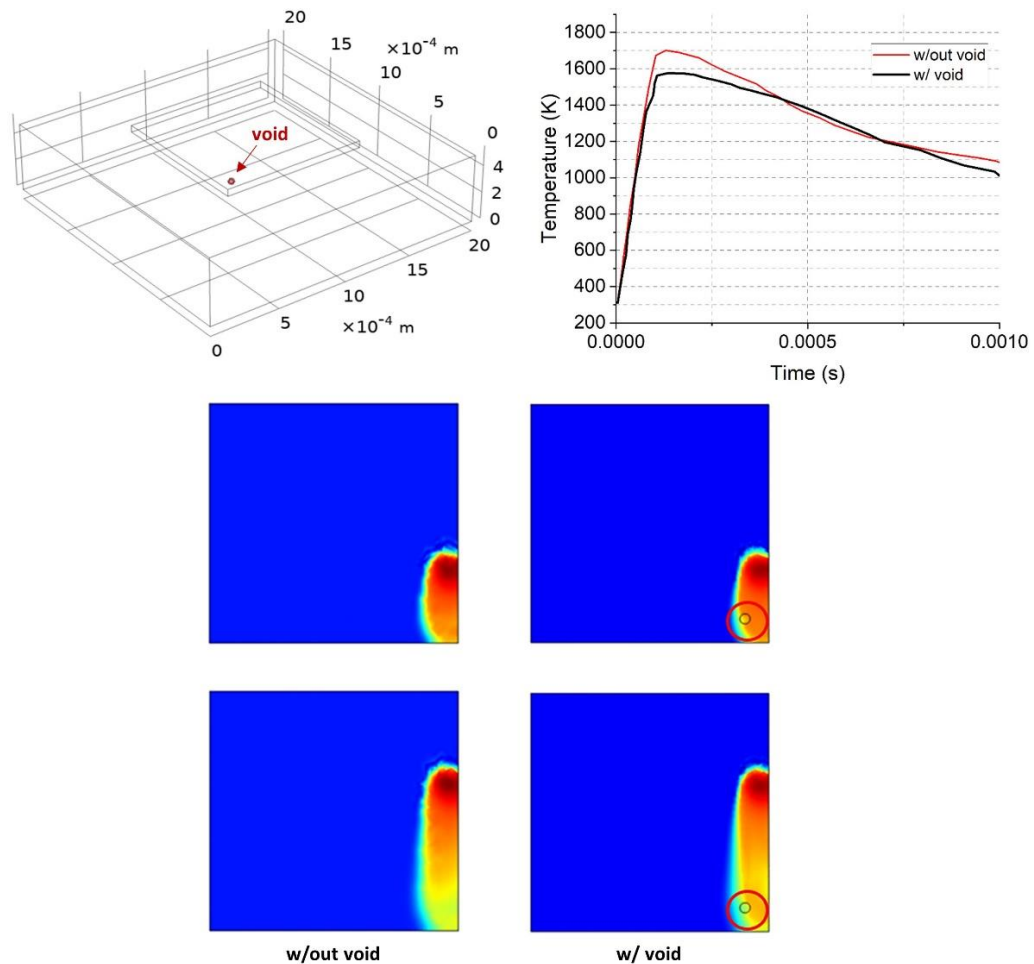
Figure 6.3: Comparison of temperature profiles at a random location in the presence and absence of a single void

According to the results presented in Figure 6.3, the peak temperature is slightly lower and starts to cool down faster in the presence of a void. It must be emphasized that, in this figure, the location of the void is random and the laser beam is not directly passing through this location. Therefore, unlike previous figures, maximum temperatures are not achieved in thermal history plots of Figure 6.3.

The results presented successfully confirmed the importance of accounting for voids in the scanning domain and their significant effect on the temperature profiles. However, introducing void elements using this approach could instantly become computationally expensive and impractical as more pores are added to the domain. Therefore, in order to increase the efficiency of the approach while expanding it to a more general framework, spatially random numbers are used in defining material properties to replicate the presence of voids in the domain during printing. Figure 6.4 compares the temperatures at a point from which the laser passes (represented by a black star) in the presence and absence of random pores during single-layer LPBF for stainless steel 316L.

Accounting for process-induced micro-voids is specifically important when modeling the thermo-mechanical behavior of materials during printing. Presence of voids in the domain can lead to local stress concentration and hence crack initiation and early failure in the printed parts. In order to take this approach one step further, statistical information on micro-voids from actual experiments can be used to replicate a more realistic presentation of voids in the domain. It must be emphasized that although introduction of voids as an input parameter in this dissertation is contrary to conventional modeling approaches, it provides a unique first approximation to high-fidelity CFD simulations while maintaining the computational efficiency of the modeling approach developed here.
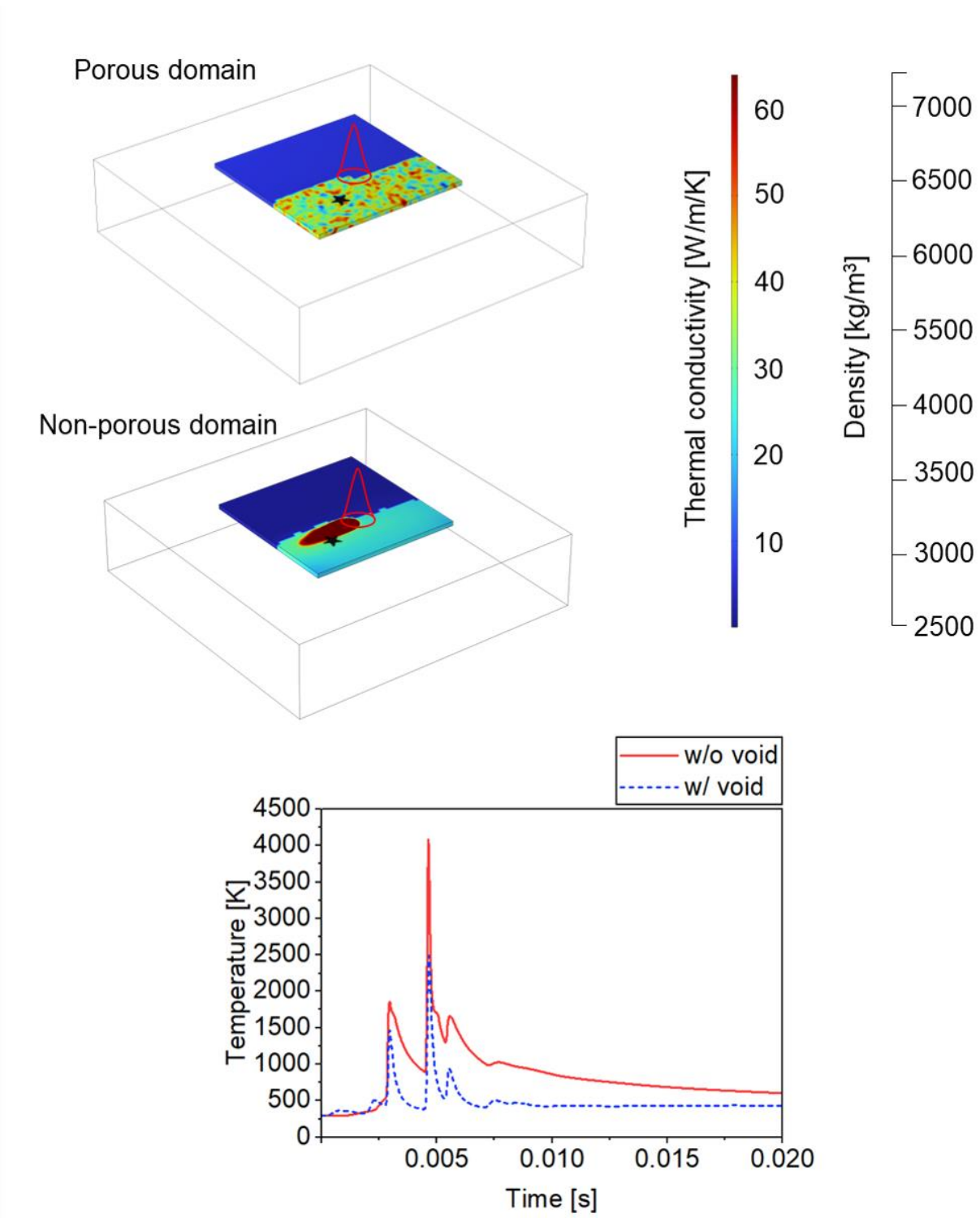
Figure 6.4: Comparison between the thermal histories at the location of a void vs. bulk material

6.4 Effect of Evaporation and Marangoni Convection on Thermo-mechanical Field

In this dissertation, the thermo-mechanical problem is modeled as a one-way coupling where the transient temperature field is computed followed by thermal expansion and stress analysis on the same FE mesh. In other words, the CTM is coupled with a mechanical model as part of the SMM approach depicted in Figure 3.1. The effects of accounting for evaporation and Marangoni convection on the thermo-mechanical response of 316L stainless steel is depicted in Figure 6.5.

Based on the results presented in Sections 6.1 and 6.2, accounting for fluid flow effects is crucial in accurate thermal modeling of LPBF processes. Therefore, it is expected that the thermo-mechanical response is also directly affected by fluid flow effects. Figure 6.5 compares the x-component of stresses as scanning of a single layer takes place and at two different locations with the representative set of process parameters tabulated in Table 4.1. A similar trend is observed in Figure 6.5 as in melt-pool sizes and peak temperatures of Figure 6.1 and Figure 6.2. This figure clearly indicates that absence of fluid flow effects leads to overestimated and unrealistically large stresses.

It must be noted that due to high computational costs of thermo-mechanical models (in the range of nanoseconds as opposed to microseconds for thermal analysis), a multi-layer simulation which accounts for heat transfer from previous layers has not been performed in this dissertation. However, this could serve as a solid foundation for further work in multi-layer and even complete part-level simulations of LPBF processes. There are approaches introduced in literature to increase the computational efficiency of the transient thermo-mechanical model for multi-layer simulations of AM processes. For instance, Zhao *et al.* [44] used two different mesh sizes

to halve the computational time: a coarser mesh for the transient heat transfer model and a finer mesh for the solid mechanics simulation.

Another approach that is commonly used to increase efficiency in part-scale thermo-mechanical models is process agglomeration in which layers are lumped into larger computational layers to reduce the total number of degrees of freedom in the problem [106]. Some examples of agglomeration approaches are agglomerated laser heat source and layer. In short, in this dissertation, the main objective is to make preliminary comparisons that illustrate the importance of fluid flow effects on the stresses during LPBF processes. Therefore, a more comprehensive study that accounts for plasticity and non-linear material behavior as well as heat transfer from lower layers can be subject of future studies.
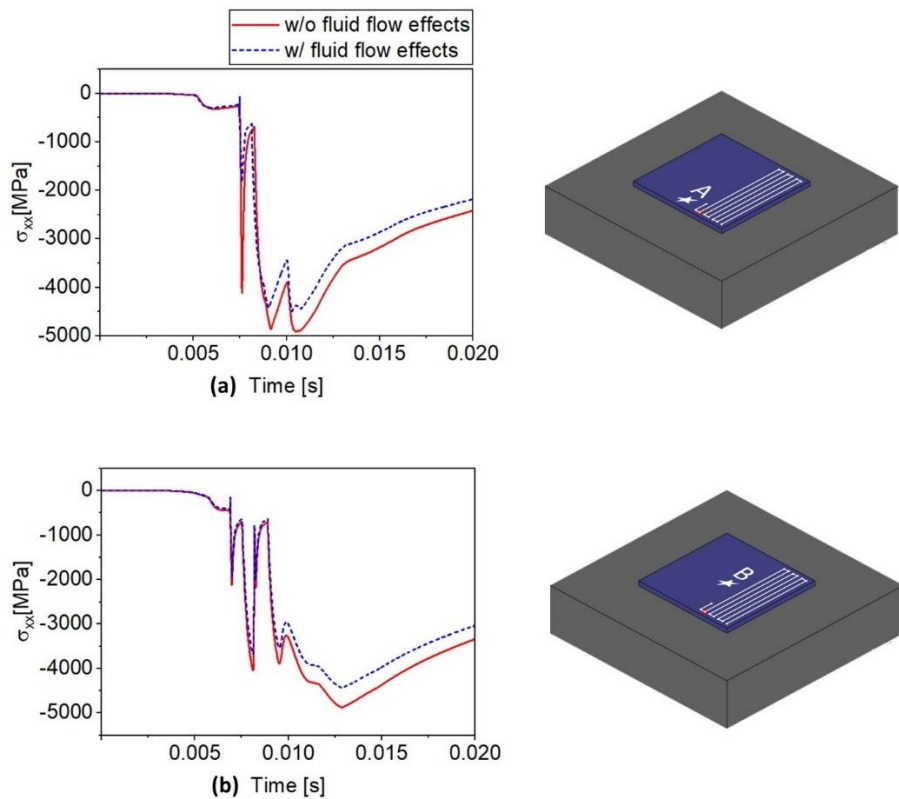
Figure 6.5: Comparison between the x stress component in the presence and absence of fluid flow effects at two locations (a) A and (b) B in the scanning domain.

Chapter 7.   Conclusions and Future Works

The primary objective of this dissertation was to develop a modeling approach that would efficiently account for micro length scale physics in multi-layer simulations of Laser Powder Bed Fusion (LPBF) processes. The presented physics-based model is accurate and efficient enough to be used for developing Reduced-Order Models (ROMs) that can then be integrated within digital twin frameworks and AI based defect control methods. An extensive literature review was performed to identify the challenges and limitations of the existing modeling approaches. Moreover, the significance of accounting for fluid flow effects on the thermal and thermo-mechanical behavior of alloys was studied and a material-dependence study was carried out to compare the response of five of the most commonly used AM alloys which include IN718, IN625, stainless steel 316L, Ti-6Al-4V, and AlSi10Mg.

7.1   Summary of This Dissertation

As the initial step, the seven major metal AM technologies as well as their mechanisms and limitations were studied. LPBF process was then identified as the most prominent metal AM technology and its drawbacks and defects were characterized. It was found that most of the defects associated with LPBF processes, namely microstructural, surface quality, and structural defects, are due to lack of control of the temperature field during printing. In other words, many of these defects are caused as a result of inaccurate prediction and control of the temperature field. Therefore, studying the thermal and thermo-mechanical behavior of the parts during printing became the goal of this research work.

After reviewing the conventional modeling approaches for LPBF processes, two major categories of thermal simulations were identified that are described in Section 2.3. These are simplified conduction-only thermal models and computationally intensive thermo-fluid models

74

(i.e. CFD simulations). While the former approach is suitable for part-scale modeling, its predictions are not very accurate with large discrepancies from experimental measurements. On the other hand, CFD simulations accurately characterize the behavior of the alloy through printing at the micro-scale but their high computational costs make them inefficient for multi-layer LPBF simulations. Therefore, the goal of this dissertation was to develop a new modeling approach, that would be used as a good first approximation to a CFD simulation while increasing the computational efficiency.

In order to satisfy this goal, the Comprehensive Thermal Model (CTM) was developed as the thermal component of the Simplified Multi-scale Modeling (SMM) approach in Chapter 3. The CTM has several unique features which include process and material dependent absorptivity, evaporation, Marangoni convection, process-induced micro-voids, latent heat, and phase transition effects as well as thermo-physical properties for bulk and powder material. In fact, implementation of process-induced micro-voids using random spatial numbers in defining material properties is a novelty of this approach which is thoroughly described in Section 3.1.7 along with the rest of the unique features discussed in Section 3.1.

As part of the SMM approach, the CTM was coupled with a linearly elastic mechanical model to study the thermomechanical behavior of the manufactured part and show the significance of accounting for micro-length scale physics on the stress state. With its accuracy and efficiency, the CTM also provides for a suitable computational tool to be used for extracting datasets and developing both a data-driven and a physics-informed Reduced-Order Model (ROM) using neural networks. Moreover, a Convolutional Neural Network (CNN) architecture and the workflow for utilizing it is proposed in Section 3.3 to be used as the foundation for developing ROMs using the proposed physics-based model.

In Chapter 4, the results of five-layer simulation using the CTM for the five alloys of interest are presented and discussed. The parameters studied include thermal signature histories, surface cooling rates, and melt-pool dimensions and the effects of material properties on the results was investigated. In order to prove the predictive capabilities of the model, the CTM is verified with experimental measurements from literature for Ti-6Al-4V and the results are presented in Chapter 5. The importance of numerical implementation of fluid flow effects in the CTM and SMM was also demonstrated in Chapter 6 and it was clearly shown that accounting for such effects is crucial in multi-layer simulations of LPBF processes. The modeling approach can also easily be extended to other metal alloys with proper definition of properties listed in Table 3.1.

7.2 Potential for Future Research

One of the major reasons contributing to the efficiency of the presented modeling approach while maintaining the essential character of the problem is simplifying assumptions used. In the CTM, the simplifying assumptions include neglecting volume shrinkage due to melting, mass loss due to evaporation, and mixing of alloys in the presence of dissimilar materials for the powder and substrate. These simplifying assumptions might have contributed to the discrepancies with experimental results presented in Chapter 5. Therefore, including the effects of such phenomena in the CTM can be further studied and conducting a systematic sensitivity analysis can be considered in future studies. Also, a quantitative analysis can be conducted to explore the sensitivity of the temperature profiles, melt-pool dimensions, and microstructural defects on the different features of the CTM, such as temperature-dependent properties, process and material dependent absorptivity, etc.

Moreover, accounting for non-linear material behavior and plastic strains in the SMM approach could result in achieving a more realistic prediction of the thermo-mechanical behavior of alloys during printing. Another possibility for future research is extending the SMM framework to multi-layer thermo-mechanical simulations to study the effect of heat transfer from lower layers on the stress state. It must be emphasized that in this dissertation, the focus was maintaining the computational efficiency of the model for multi-layer modeling and accounting for such physics would have hindered the fundamental objective of this research work.

Although computer simulations are often used as an efficient substitute for experiments, calibrating the presented model with experimental measurements for each material system would be very useful. Currently, the CTM is verified with experimental measurements provided in literature for Ti-6Al-4V only. Extending this to the rest of the alloys while calibrating temperature and stress predictions with experimental measurements could be subject of future studies. Also, incorporating statistical information on process-induced micro-voids obtained from experiments (as discussed in Section 3.1.7) can help with increasing the practicality of the presented framework and is worth further studying.

Moreover, as described in Section 2.3.4, the basis for modeling the microstructure or the grain structural evolution during LPBF processes is a well-defined thermal field. Therefore, the temperature field predictions of the CTM can be fed into microstructure simulations in the future studies. Another possibility of future work is investigating how the presented model can be efficiently extended to actual part-scale simulations (with hundreds of layers and much larger scanning domains). Due to limited computational resources, the presented model was limited to five-layer simulations of $1\ mm\ \times 1\ mm$ powder domains only. However, scaling the model up

to structural level simulations would require access to parallel computing techniques and High-Performance Computing (HPC).

Utilizing HPC can also benefit developing ROMs, specifically data-driven ROMs, by paving the way for collecting datasets in a more efficient manner. The collected datasets can also be used in developing process maps for the AM process. Constructing process maps would help researchers visually identify a suitable range of process parameters (i.e., a process window) for achieving parts with optimized qualities such as surface roughness, density, residual stresses, etc. Moreover, full development of ROMs and their integration within the digital twin framework would be crucial in efficiently printing sound parts with optimized mechanical properties and minimal qualification testing.

References

[1]   A. Vafadar, F. Guzzomi, A. Rassau, K. Hayward, Advances in metal additive manufacturing: A review of common processes, industrial applications, and current challenges, Applied Sciences (Switzerland). 11 (2021) 1–33. https://doi.org/10.3390/app11031213.

[2]   F.P.W. Melchels, J. Feijen, D.W. Grijpma, A review on stereolithography and its applications in biomedical engineering, Biomaterials. 31 (2010) 6121–6130. https://doi.org/10.1016/j.biomaterials.2010.04.050.

[3]   M.A. Saccone, Vat Photopolymerization Additive Manufacturing of Functional Materials: from Batteries to Metals and Alloys, California Institute of Technology, 2022.

[4]   G.H. Loh, E. Pei, J. Gonzalez-Gutierrez, M. Monzón, An overview of material extrusion troubleshooting, Applied Sciences (Switzerland). 10 (2020). https://doi.org/10.3390/app10144776.

[5]   J.S. Lim, W.J. Oh, C.M. Lee, D.H. Kim, Selection of effective manufacturing conditions for directed energy deposition process using machine learning methods, Sci Rep. 11 (2021). https://doi.org/10.1038/s41598-021-03622-z.

[6]   Introduction to 3D printing - additive processes, (2018).

[7]   E. Feilden, F. Giuliani, L. Vandeperre, E. Saiz, Additive Manufacturing of Ceramics and Ceramic Composites via Robocasting, n.d.

[8]   I. Gibson, D. Rosen, B. Stucker, M. Khorasani, Additive Manufacturing Technologies, n.d.

[9]   J.P. Oliveira, A.D. LaLonde, J. Ma, Processing parameters in laser powder bed fusion metal additive manufacturing, Mater Des. 193 (2020). https://doi.org/10.1016/j.matdes.2020.108762.

[10]   A. Salmi, F. Calignano, M. Galati, E. Atzeni, An integrated design methodology for components produced by laser powder bed fusion (L-PBF) process, Virtual Phys Prototyp. 13 (2018) 191–202. https://doi.org/10.1080/17452759.2018.1442229.

[11]   L.E. Criales, Y.M. Arısoy, B. Lane, S. Moylan, A. Donmez, T. Özel, Laser powder bed fusion of nickel alloy 625: Experimental investigations of effects of process parameters on

melt pool size and shape with spatter analysis, Int J Mach Tools Manuf. 121 (2017) 22–36. https://doi.org/10.1016/j.ijmachtools.2017.03.004.

[12]   J.G. Santos Macías, L. Zhao, D. Tingaud, B. Bacroix, G. Pyka, C. van der Rest, L. Ryelandt, A. Simar, Hot isostatic pressing of laser powder bed fusion AlSi10Mg: parameter identification and mechanical properties, J Mater Sci. 57 (2022) 9726–9740. https://doi.org/10.1007/s10853-022-07027-9.

[13]   S. Gorsse, C. Hutchinson, M. Gouné, R. Banerjee, Additive manufacturing of metals: a brief review of the characteristic microstructures and properties of steels, Ti-6Al-4V and high-entropy alloys, Sci Technol Adv Mater. 18 (2017) 584–610. https://doi.org/10.1080/14686996.2017.1361305.

[14]   S. Sanchez, P. Smith, Z. Xu, G. Gaspard, C.J. Hyde, W.W. Wits, I.A. Ashcroft, H. Chen, A.T. Clare, Powder Bed Fusion of nickel-based superalloys: A review, Int J Mach Tools Manuf. 165 (2021). https://doi.org/10.1016/j.ijmachtools.2021.103729.

[15]   S. Cooke, K. Ahmadi, S. Willerth, R. Herring, Metal additive manufacturing: Technology, metallurgy and modelling, J Manuf Process. 57 (2020) 978–1003. https://doi.org/10.1016/j.jmapro.2020.07.025.

[16]   J.P. Oliveira, A.D. LaLonde, J. Ma, Processing parameters in laser powder bed fusion metal additive manufacturing, Mater Des. 193 (2020). https://doi.org/10.1016/j.matdes.2020.108762.

[17]   H. Rezaeifar, M. Elbestawi, Porosity formation mitigation in laser powder bed fusion process using a control approach, Opt Laser Technol. 147 (2022). https://doi.org/10.1016/j.optlastec.2021.107611.

[18]   R. Li, J. Liu, Y. Shi, L. Wang, W. Jiang, Balling behavior of stainless steel and nickel powder during selective laser melting process, International Journal of Advanced Manufacturing Technology. 59 (2012) 1025–1035. https://doi.org/10.1007/s00170-011-3566-1.

[19]   X. Song, S. Feih, W. Zhai, C.N. Sun, F. Li, R. Maiti, J. Wei, Y. Yang, V. Oancea, L. Romano Brandt, A.M. Korsunsky, Advances in additive manufacturing process simulation: Residual stresses and distortion predictions in complex metallic components, Mater Des. 193 (2020). https://doi.org/10.1016/j.matdes.2020.108779.

[20] C. Panwisawas, Y.T. Tang, R.C. Reed, Metal 3D printing as a disruptive technology for superalloys, Nat Commun. 11 (2020). https://doi.org/10.1038/s41467-020-16188-7.

[21] B. Schoinochoritis, D. Chantzis, K. Salonitis, Simulation of metallic powder bed additive manufacturing processes with the finite element method: A critical review, Proc Inst Mech Eng B J Eng Manuf. 231 (2017) 96–117. https://doi.org/10.1177/0954405414567522.

[22] Z. Luo, Y. Zhao, A survey of finite element analysis of temperature and thermal stress fields in powder bed fusion Additive Manufacturing, Addit Manuf. 21 (2018) 318–332. https://doi.org/10.1016/j.addma.2018.03.022.

[23] L.E. Loh, C.K. Chua, W.Y. Yeong, J. Song, M. Mapar, S.L. Sing, Z.H. Liu, D.Q. Zhang, Numerical investigation and an effective modelling on the Selective Laser Melting (SLM) process with aluminium alloy 6061, Int J Heat Mass Transf. 80 (2015) 288–300. https://doi.org/10.1016/j.ijheatmasstransfer.2014.09.014.

[24] A. Masmoudi, R. Bolot, C. Coddet, Investigation of the laser-powder-atmosphere interaction zone during the selective laser melting process, J Mater Process Technol. 225 (2015) 122–132. https://doi.org/10.1016/j.jmatprotec.2015.05.008.

[25] A. Foroozmehr, M. Badrossamay, E. Foroozmehr, S. Golabi, Finite Element Simulation of Selective Laser Melting process considering Optical Penetration Depth of laser in powder bed, Mater Des. 89 (2016) 255–263. https://doi.org/10.1016/j.matdes.2015.10.002.

[26] J. Yin, H. Zhu, L. Ke, W. Lei, C. Dai, D. Zuo, Simulation of temperature distribution in single metallic powder layer for laser micro-sintering, Comput Mater Sci. 53 (2012) 333–339. https://doi.org/10.1016/j.commatsci.2011.09.012.

[27] H. Hu, X. Ding, L. Wang, Numerical analysis of heat transfer during multi-layer selective laser melting of AlSi10Mg, Optik (Stuttg). 127 (2016) 8883–8891. https://doi.org/10.1016/j.ijleo.2016.06.115.

[28] J. Coleman, A. Plotkowski, B. Stump, N. Raghavan, A.S. Sabau, M.J.M. Krane, J. Heigel, R.E. Ricker, L. Levine, S.S. Babu, Sensitivity of thermal predictions to uncertain surface tension data in laser additive manufacturing, J Heat Transfer. 142 (2020). https://doi.org/10.1115/1.4047916.

[29] A. Aggarwal, S. Patel, A. Kumar, Selective Laser Melting of 316L Stainless Steel: Physics of Melting Mode Transition and Its Influence on Microstructural and Mechanical Behavior, JOM. 71 (2019) 1105–1116. https://doi.org/10.1007/s11837-018-3271-8.

[30] H. Qi, J. Mazumder, H. Ki, Numerical simulation of heat transfer and fluid flow in coaxial laser cladding process for direct metal deposition, J Appl Phys. 100 (2006). https://doi.org/10.1063/1.2209807.

[31] T. Heeling, M. Cloots, K. Wegener, Melt pool simulation for the evaluation of process parameters in selective laser melting, Addit Manuf. 14 (2017) 116–125. https://doi.org/10.1016/j.addma.2017.02.003.

[32] H.C. Basoalto, C. Panwisawas, Y. Sovani, M.J. Anderson, R.P. Turner, B. Saunders, J.W. Brooks, A computational study on the three-dimensional printability of precipitate-strengthened nickel-based superalloys, Source: Proceedings: Mathematical, Physical and Engineering Sciences. 474 (2018) 1–23. https://doi.org/10.2307/26583561.

[33] Y.S. Lee, W. Zhang, Modeling of heat transfer, fluid flow and solidification microstructure of nickel-base superalloy fabricated by laser powder bed fusion, Addit Manuf. 12 (2016) 178–188. https://doi.org/10.1016/j.addma.2016.05.003.

[34] T. Mukherjee, H.L. Wei, A. De, T. DebRoy, Heat and fluid flow in additive manufacturing—Part I: Modeling of powder bed fusion, Comput Mater Sci. 150 (2018) 304–313. https://doi.org/10.1016/j.commatsci.2018.04.022.

[35] T. Mukherjee, H.L. Wei, A. De, T. DebRoy, Heat and fluid flow in additive manufacturing – Part II: Powder bed fusion of stainless steel, and titanium, nickel and aluminum base alloys, Comput Mater Sci. 150 (2018) 369–380. https://doi.org/10.1016/j.commatsci.2018.04.027.

[36] K. Karayagiz, A. Elwany, G. Tapia, B. Franco, L. Johnson, J. Ma, I. Karaman, R. Arróyave, Numerical and experimental analysis of heat distribution in the laser powder bed fusion of Ti-6Al-4V, IISE Trans. 51 (2019) 136–152. https://doi.org/10.1080/24725854.2018.1461964.

[37] S.H. Nikam, J. Quinn, S. McFadden, A simplified thermal approximation method to include the effects of Marangoni convection in the melt pools of processes that involve moving point heat sources, Numeri Heat Transf A Appl. 79 (2021) 537–552. https://doi.org/10.1080/10407782.2021.1872257.

[38] L. Ladani, J. Romano, W. Brindley, S. Burlatsky, Effective liquid conductivity for improved simulation of thermal transport in laser beam melting powder bed technology, Addit Manuf. 14 (2017) 13–23. https://doi.org/10.1016/j.addma.2016.12.004.

[39] J. Li, X. Zhou, M. Brochu, N. Provatas, Y.F. Zhao, Solidification microstructure simulation of Ti-6Al-4V in metal additive manufacturing: A review, Addit Manuf. 31 (2020). https://doi.org/10.1016/j.addma.2019.100989.

[40] Y. Lu, G. Sun, X. Xiao, J. Mazumder, Online Stress Measurement During Laser-aided Metallic Additive Manufacturing, Sci Rep. 9 (2019). https://doi.org/10.1038/s41598-019-39849-0.

[41] B. Cheng, S. Shrestha, K. Chou, Stress and deformation evaluations of scanning strategy effect in selective laser melting, Addit Manuf. 12 (2016) 240–251. https://doi.org/10.1016/j.addma.2016.05.007.

[42] T. Mukherjee, W. Zhang, T. DebRoy, An improved prediction of residual stresses and distortion in additive manufacturing, Comput Mater Sci. 126 (2017) 360–372. https://doi.org/10.1016/j.commatsci.2016.10.003.

[43] B.K. Panda, S. Sahoo, Thermo-mechanical modeling and validation of stress field during laser powder bed fusion of AlSi10Mg built part, Results Phys. 12 (2019) 1372–1381. https://doi.org/10.1016/j.rinp.2019.01.002.

[44] X. Zhao, A. Iyer, P. Promoppatum, S.C. Yao, Numerical modeling of the thermal behavior and residual stress in the direct metal laser sintering process of titanium alloy products, Addit Manuf. 14 (2017) 126–136. https://doi.org/10.1016/j.addma.2016.10.005.

[45] F. Chen, W. Yan, High-fidelity modelling of thermal stress for additive manufacturing by linking thermal-fluid and mechanical models, Mater Des. 196 (2020). https://doi.org/10.1016/j.matdes.2020.109185.

[46] C. Körner, M. Markl, J.A. Koepf, Modeling and Simulation of Microstructure Evolution for Additive Manufacturing of Metals: A Critical Review, Metall Mater Trans A Phys Metall Mater Sci. 51 (2020) 4970–4983. https://doi.org/10.1007/s11661-020-05946-3.

[47] S. DeWitt, S. Rudraraju, D. Montiel, W.B. Andrews, K. Thornton, PRISMS-PF: A general framework for phase-field modeling with a matrix-free finite element method, NPJ Comput Mater. 6 (2020). https://doi.org/10.1038/s41524-020-0298-5.

[48] MOOSE Phase Field Module, (n.d.). https://mooseframework.inl.gov/modules/phase_field/ (accessed October 27, 2022).

[49] M. Rolchigo, S.T. Reeve, B. Stump, G.L. Knapp, J. Coleman, A. Plotkowski, J. Belak, ExaCA: A performance portable exascale cellular automata application for alloy

solidification modeling, Comput Mater Sci. 214 (2022).
https://doi.org/10.1016/j.commatsci.2022.111692.

[50]   SPPARKS Kinetic Monte Carlo Simulator, (n.d.). https://spparks.github.io/ (accessed October 27, 2022).

[51]   PhasePot: Simulation Software for Engineers & Scientists, (n.d.). https://phasepot.com/ (accessed October 27, 2022).

[52]   D. Rosenthal, The Theory of Moving Sources of Heat and its Application to Metal Treatments, ASME, Cambridge, 1946.

[53]   T.V. Eagar, N.-S. Tsai, Temperature Fields Produced by Traveling Distributed Heat Sources, n.d.

[54]   J. Goldak, A. Chakravarti, M. Bibby, A New Finite Element Model for Welding Heat Sources, n.d.

[55]   S.A. Khairallah, A.T. Anderson, A. Rubenchik, W.E. King, Laser powder-bed fusion additive manufacturing: Physics of complex melt flow and formation mechanisms of pores, spatter, and denudation zones, Acta Mater. 108 (2016) 36–45. https://doi.org/10.1016/j.actamat.2016.02.014.

[56]   H.L. Wei, T. Mukherjee, W. Zhang, J.S. Zuback, G.L. Knapp, A. De, T. DebRoy, Mechanistic models for additive manufacturing of metallic components, Prog Mater Sci. 116 (2021). https://doi.org/10.1016/j.pmatsci.2020.100703.

[57]   P. Promoppatum, S.C. Yao, P.C. Pistorius, A.D. Rollett, A Comprehensive Comparison of the Analytical and Numerical Prediction of the Thermal History and Solidification Microstructure of Inconel 718 Products Made by Laser Powder-Bed Fusion, Engineering. 3 (2017) 685–694. https://doi.org/10.1016/J.ENG.2017.05.023.

[58]   Z. Gan, O.L. Kafka, N. Parab, C. Zhao, L. Fang, O. Heinonen, T. Sun, W.K. Liu, Universal scaling laws of keyhole stability and porosity in 3D printing of metals, Nat Commun. 12 (2021). https://doi.org/10.1038/s41467-021-22704-0.

[59]   M. Matsumoto, M. Shiomi, K. Osakada, F. Abe, Finite element analysis of single layer forming on metallic powder bed in rapid prototyping by selective laser processing, 2002.

[60]   H.L. Wei, T. Mukherjee, W. Zhang, J.S. Zuback, G.L. Knapp, A. De, T. DebRoy, Mechanistic models for additive manufacturing of metallic components, Prog Mater Sci. 116 (2021). https://doi.org/10.1016/j.pmatsci.2020.100703.

[61] S.D. Proell, W.A. Wall, C. Meier, On phase change and latent heat models in metal additive manufacturing process simulation, (2019). https://doi.org/10.1186/s40323-020-00158-1.

[62] X. Qi, G. Chen, Y. Li, X. Cheng, C. Li, Applying Neural-Network-Based Machine Learning to Additive Manufacturing: Current Applications, Challenges, and Future Perspectives, Engineering. 5 (2019) 721–729. https://doi.org/10.1016/j.eng.2019.04.012.

[63] C. Wang, X.P. Tan, S.B. Tor, C.S. Lim, Machine learning in additive manufacturing: State-of-the-art and perspectives, Addit Manuf. 36 (2020). https://doi.org/10.1016/j.addma.2020.101538.

[64] Y. Zhang, G.S. Hong, D. Ye, K. Zhu, J.Y.H. Fuh, Extraction and evaluation of melt pool, plume and spatter information for powder-bed fusion AM process monitoring, Mater Des. 156 (2018) 458–469. https://doi.org/10.1016/j.matdes.2018.07.002.

[65] B. Yuan, G.M. Guss, A.C. Wilson, S.P. Hau-Riege, P.J. DePond, S. McMains, M.J. Matthews, B. Giera, Machine-Learning-Based Monitoring of Laser Powder Bed Fusion, Adv Mater Technol. 3 (2018). https://doi.org/10.1002/admt.201800136.

[66] A. Paul, M. Mozaffar, Z. Yang, W. Liao, A. Choudhary, J. Cao, A. Agrawal, A real-time iterative machine learning approach for temperature profile prediction in additive manufacturing processes, (2019). http://arxiv.org/abs/1907.12953.

[67] E. Popova, T.M. Rodgers, X. Gong, A. Cecen, J.D. Madison, S.R. Kalidindi, Process-Structure Linkages Using a Data Science Approach: Application to Simulated Additive Manufacturing Data, Integr Mater Manuf Innov. 6 (2017) 54–68. https://doi.org/10.1007/s40192-017-0088-1.

[68] C. Kamath, Data mining and statistical inference in selective laser melting, International Journal of Advanced Manufacturing Technology. 86 (2016) 1659–1677. https://doi.org/10.1007/s00170-015-8289-2.

[69] T.W. Heo, S.A. Khairallah, R. Shi, J. Berry, A. Perron, N.P. Calta, A.A. Martin, N.R. Barton, J. Roehling, T. Roehling, J.L. Fattebert, A. Anderson, A.L. Nichols, S. Wopschall, W.E. King, J.T. McKeown, M.J. Matthews, A mesoscopic digital twin that bridges length and time scales for control of additively manufactured metal microstructures, JPhys Materials. 4 (2021). https://doi.org/10.1088/2515-7639/abeef8.

[70]   A. Khadilkar, J. Wang, R. Rai, Deep learning–based stress prediction for bottom-up SLA
        3D printing process, International Journal of Advanced Manufacturing Technology. 102
        (2019) 2555–2569. https://doi.org/10.1007/s00170-019-03363-4.

[71]   J. Wang, S. Das, R. Rai, C. Zhou, Data-driven simulation for fast prediction of pull-up
        process in bottom-up stereo-lithography, CAD Computer Aided Design. 99 (2018) 29–42.
        https://doi.org/10.1016/j.cad.2018.02.002.

[72]   A.R. Sofi, B. Ravani, Sub-Second Prediction of the Heatmap of Powder-Beds in Additive
        Manufacturing Using Deep Encoder–Decoder Convolutional Neural Networks, J Comput
        Inf Sci Eng. 23 (2023). https://doi.org/10.1115/1.4054559.

[73]   M. Raissi, P. Perdikaris, G.E. Karniadakis, Physics-informed neural networks: A deep
        learning framework for solving forward and inverse problems involving nonlinear partial
        differential equations, J Comput Phys. 378 (2019) 686–707.
        https://doi.org/10.1016/j.jcp.2018.10.045.

[74]   X. Zhao, Z. Gong, Y. Zhang, W. Yao, X. Chen, Physics-informed Convolutional Neural
        Networks for Temperature Field Prediction of Heat Source Layout without Labeled Data,
        (2021). http://arxiv.org/abs/2109.12482.

[75]   D. Gunasegaram, A.B. Murphy, Towards a true digital twin for the metal Additive
        Manufacturing process, 2019. https://www.researchgate.net/publication/336568564.

[76]   T. DebRoy, W. Zhang, J. Turner, S.S. Babu, Building digital twins of 3D printing
        machines, Scr Mater. 135 (2017) 119–124.
        https://doi.org/10.1016/j.scriptamat.2016.12.005.

[77]   N. Peter, Z. Pitts, S. Thompson, A. Saharan, Benchmarking build simulation software for
        laser powder bed fusion of metals, Addit Manuf. 36 (2020).
        https://doi.org/10.1016/j.addma.2020.101531.

[78]   Ansys Additive Print, (2022). https://www.ansys.com/products/additive/ansys-additive-
        print (accessed October 25, 2022).

[79]   Atlas 3D, (2022). https://atlas3d.xyz/ (accessed October 25, 2022).

[80]   Amphyon: Metal additive manufacturing simulation software, (n.d.).
        https://www.oqton.com/amphyon/ (accessed October 25, 2022).

[81]   Simulating Additive Manufacturing with Simufact Additive, (n.d.).
        https://www.simufact.com/simufact-additive.html (accessed October 25, 2022).

[82] Fusion 360 with Netfabb: Software for additive manufacturing, design, and simulation, (n.d.). https://www.autodesk.com/products/netfabb (accessed October 25, 2022).

[83] FLOW-3D AM, (n.d.). https://www.flow3d.com/products/flow3d-am/ (accessed October 25, 2022).

[84] LiveLink ™ for MATLAB ® User's Guide, 2009.

[85] S.T. Strayer, W.J.F. Templeton, F.X. Dugast, S.P. Narra, A.C. To, Accelerating High-Fidelity Thermal Process Simulation of Laser Powder Bed Fusion via the Computational Fluid Dynamics Imposed Finite Element Method (CIFEM), Additive Manufacturing Letters. 3 (2022) 100081. https://doi.org/10.1016/j.addlet.2022.100081.

[86] K. Mills, Recommended Values of Thermophysical Properties for Selected Commercial Alloys, Woodland Publishing, Sawston, Cambridge, 2002.

[87] J.J. Radice, P.J.J. Midn, / C Andrew, T. Capt, J. Watkins, Numerical Modeling of Heat Transfer and Damage Evolution due to HEL Irradiation, n.d.

[88] Bjorn Sjodin, How to Generate Randomized Inhomogeneous Material Data, COMSOL Blog. (2017). https://www.comsol.com/blogs/how-to-generate-randomized-inhomogeneous-material-data/ (accessed April 14, 2022).

[89] A. du Plessis, Effects of process parameters on porosity in laser powder bed fusion revealed by X-ray tomography, Addit Manuf. 30 (2019). https://doi.org/10.1016/j.addma.2019.100871.

[90] G. Kasperovich, J. Haubrich, J. Gussone, G. Requena, Correlation between porosity and processing parameters in TiAl6V4 produced by selective laser melting, Mater Des. 105 (2016) 160–170. https://doi.org/10.1016/j.matdes.2016.05.070.

[91] J. Ye, S.A. Khairallah, A.M. Rubenchik, M.F. Crumb, G. Guss, J. Belak, M.J. Matthews, Energy Coupling Mechanisms and Scaling Behavior Associated with Laser Powder Bed Fusion Additive Manufacturing, Adv Eng Mater. 21 (2019). https://doi.org/10.1002/adem.201900185.

[92] S. Safdar, A.J. Pinkerton, L. Li, M.A. Sheikh, P.J. Withers, An anisotropic enhanced thermal conductivity approach for modelling laser melt pools for Ni-base super alloys, Appl Math Model. 37 (2013) 1187–1195. https://doi.org/10.1016/j.apm.2012.03.028.

[93] A. Kumar, C.P. Paul, A.S. Padiyar, P. Bhargava, G. Mundra, L.M. Kukreja, Numerical simulation of laser rapid manufacturing of multi-layer thin wall using an improved mass

addition approach, Numeri Heat Transf A Appl. 65 (2014) 885–910.
https://doi.org/10.1080/10407782.2013.850968.

[94]   I.A. Roberts, C.J. Wang, R. Esterlein, M. Stanford, D.J. Mynors, A three-dimensional
        finite element analysis of the temperature field during laser melting of metal powders in
        additive layer manufacturing, Int J Mach Tools Manuf. 49 (2009) 916–923.
        https://doi.org/10.1016/j.ijmachtools.2009.07.004.

[95]   H. Hu, X. Ding, L. Wang, Numerical analysis of heat transfer during multi-layer selective
        laser melting of AlSi10Mg, Optik (Stuttg). 127 (2016) 8883–8891.
        https://doi.org/10.1016/j.ijleo.2016.06.115.

[96]   Mark M. Rashid, ECI 201: INTRODUCTION TO THE THEORY OF ELASTICITY, n.d.

[97]   D. Peckner, I.M. Bernstein, Handbook of Stainless Steels, MacGraw-Hill, Inc., 1977.

[98]   N.E. Hodge, R.M. Ferencz, J.M. Solberg, Implementation of a thermomechanical model
        for the simulation of selective laser melting, Comput Mech. 54 (2014) 33–51.
        https://doi.org/10.1007/s00466-014-1024-2.

[99]   L. Parry, I.A. Ashcroft, R.D. Wildman, Understanding the effect of laser scan strategy on
        residual stress in selective laser melting through thermo-mechanical simulation, Addit
        Manuf. 12 (2016) 1–15. https://doi.org/10.1016/j.addma.2016.05.014.

[100]   X. Liu, K. Wang, P. Hu, X. He, B. Yan, X. Zhao, Formability, microstructure and
        properties of inconel 718 superalloy fabricated by selective laser melting additive
        manufacture technology, Materials. 14 (2021) 1–18. https://doi.org/10.3390/ma14040991.

[101]   G.A. Dzukey, K. Yang, Process Parameter Optimization for Selective Laser Melting of
        316L Stainless Steel Material using Taguchi's Statistical Design of Experiment Procedure,
        International Journal of Engineering and Technology. 11 (2019) 6–13.
        https://doi.org/10.21817/ijet/2019/v11i1/191101014.

[102]   D.S. Nguyen, H.S. Park, C.M. Lee, Optimization of selective laser melting process
        parameters for Ti-6Al-4V alloy manufacturing using deep learning, J Manuf Process. 55
        (2020) 230–235. https://doi.org/10.1016/j.jmapro.2020.04.014.

[103]   N. Read, W. Wang, K. Essa, M.M. Attallah, Selective laser melting of AlSi10Mg alloy:
        Process optimisation and mechanical properties development, Mater Des. 65 (2015) 417–
        424. https://doi.org/10.1016/j.matdes.2014.09.044.

[104] P.A. Hooper, Melt pool temperature and cooling rates in laser powder bed fusion, Addit Manuf. 22 (2018) 548–559. https://doi.org/10.1016/j.addma.2018.05.032.

[105] P. Yuan, D. Gu, Molten pool behaviour and its physical mechanism during selective laser melting of TiC/AlSi10Mg nanocomposites: Simulation and experiments, J Phys D Appl Phys. 48 (2015). https://doi.org/10.1088/0022-3727/48/3/035303.

[106] R.K. Ganeriwala, M. Strantza, W.E. King, B. Clausen, T.Q. Phan, L.E. Levine, D.W. Brown, N.E. Hodge, Evaluation of a thermomechanical model for prediction of residual stress during laser powder bed fusion of Ti-6Al-4V, Addit Manuf. 27 (2019) 489–502. https://doi.org/10.1016/j.addma.2019.03.034.